



# The Relation between Globular Cluster Systems and Supermassive Black Holes in Spiral Galaxies. III. The Link to the M •-M \* Correlation

Rosa A. González-Lópezlira, Luis Lomelí-Núñez, Yasna Ordenes-Briceño, Laurent Loinard, Stephen Gwyn, Karla Alamo-Martínez, Gustavo Bruzual, Ariane Lançon, Thomas H. Puzia

## ► To cite this version:

Rosa A. González-Lópezlira, Luis Lomelí-Núñez, Yasna Ordenes-Briceño, Laurent Loinard, Stephen Gwyn, et al.. The Relation between Globular Cluster Systems and Supermassive Black Holes in Spiral Galaxies. III. The Link to the M •-M \* Correlation. *The Astrophysical Journal*, 2022, 941, 10.3847/1538-4357/ac982e . insu-03926795

HAL Id: insu-03926795

<https://insu.hal.science/insu-03926795>

Submitted on 6 Jan 2023

**HAL** is a multi-disciplinary open access archive for the deposit and dissemination of scientific research documents, whether they are published or not. The documents may come from teaching and research institutions in France or abroad, or from public or private research centers.

L'archive ouverte pluridisciplinaire **HAL**, est destinée au dépôt et à la diffusion de documents scientifiques de niveau recherche, publiés ou non, émanant des établissements d'enseignement et de recherche français ou étrangers, des laboratoires publics ou privés.



Distributed under a Creative Commons Attribution 4.0 International License



# The Relation between Globular Cluster Systems and Supermassive Black Holes in Spiral Galaxies. III. The Link to the $M$ - $M_*$ Correlation

Rosa A. González-Lópezlira<sup>1</sup> , Luis Lomelí-Núñez<sup>2,3</sup> , Yasna Ordenes-Briceño<sup>4</sup> , Laurent Loinard<sup>3</sup> , Stephen Gwyn<sup>5</sup> , Karla Alamo-Martínez<sup>6</sup> , Gustavo Bruzual<sup>3</sup> , Ariane Lançon<sup>7</sup> , and Thomas H. Puzia<sup>4</sup>

<sup>1</sup> Instituto de Radioastronomía y Astrofísica, UNAM, Campus Morelia, Michoacan, C.P. 58089, Mexico; [r.gonzalez@irya.unam.mx](mailto:r.gonzalez@irya.unam.mx)

<sup>2</sup> Instituto Nacional de Astrofísica, Óptica y Electrónica, Luis Enrique Erro 1, Tonantzintla, Puebla, C.P. 72840, Mexico

<sup>3</sup> Instituto de Radioastronomía y Astrofísica, UNAM, Campus Morelia, Michoacan, C.P. 58089, Mexico

<sup>4</sup> Instituto de Astrofísica, Pontificia Universidad Católica de Chile, Av. Vicuña Mackenna 4860, 7820436 Macul, Santiago, Chile

<sup>5</sup> Herzberg Institute of Astrophysics, National Research Council of Canada, Victoria, BC V9E 2E7, Canada

<sup>6</sup> Departamento de Física, División de Ciencias e Ingenierías, Universidad de Guanajuato, 37150, León, Mexico

<sup>7</sup> Observatoire Astronomique de Strasbourg, Université de Strasbourg, CNRS, UMR 7550, 11 rue de l'Université, F-67000 Strasbourg, France  
*Received 2021 August 8; revised 2022 September 14; accepted 2022 October 3; published 2022 December 12*

## Abstract

We continue to explore the relationship between the total number of globular clusters (GCs),  $N_{\text{GC}}$ , and the central black hole mass,  $M_*$ , in spiral galaxies. We present here results for the Sab galaxies NGC 3368, NGC 4736 (M94), and NGC 4826 (M64), and the Sm galaxy NGC 4395. The GC candidate selection is based on the  $(u^* - i')$  versus  $(i' - K_s)$  color–color diagram, and  $i'$ -band shape parameters. We determine the  $M_*$  versus  $N_{\text{GC}}$  correlation for these spirals, plus NGC 4258, NGC 253, M104, M81, M31, and the Milky Way. We also redetermine the correlation for the elliptical sample in Harris et al., with updated galaxy types from Sahu et al. Additionally, we derive the total stellar galaxy mass,  $M_*$ , from its two-slope correlation with  $N_{\text{GC}}$ , and fit  $M_*$  versus  $M_*$  for both spirals and ellipticals. We obtain  $\log M_* \propto (1.01 \pm 0.13) \log N_{\text{GC}}$  for ellipticals, and  $\log M_* \propto (1.64 \pm 0.24) \log N_{\text{GC}}$  for late-type galaxies (LTGs). The linear  $M_*$  versus  $N_{\text{GC}}$  correlation in ellipticals could be due to statistical convergence through mergers, unlike the much steeper correlation for LTGs. However, in the  $M_*$  versus total stellar mass ( $M_*$ ) parameter space, with  $M_*$  derived from its correlation with  $N_{\text{GC}}$ ,  $M_* \propto (1.48 \pm 0.18) \log M_*$  for ellipticals, and  $M_* \propto (1.21 \pm 0.16) \log M_*$  for LTGs. The observed agreement between ellipticals and LTGs in this parameter space may imply that black holes and galaxies coevolve through *calm* accretion, active galactic nuclei feedback, and other secular processes.

*Unified Astronomy Thesaurus concepts:* Galaxy formation (595); Galaxy evolution (594); Spiral galaxies (1560); Globular star clusters (656); Star clusters (1567); Classical black holes (249); Black holes (162)

*Supporting material:* machine-readable tables

## 1. Introduction

It is widely accepted that all massive galaxies contain a supermassive black hole (SMBH). In spheroidal systems, the masses of the SMBHs,  $M_*$ , correlate with other properties of their host galaxies: the bulge luminosity (the  $M_*$ - $L_{\text{bulge}}$  relation, e.g., Kormendy 1993; Kormendy & Richstone 1995), the bulge mass (the  $M_*$ - $M_{\text{bulge}}$  relation, e.g., Dressler 1989; Magorrian et al. 1998), the bulge stellar velocity dispersion (the  $M_*$ - $\sigma_*$  relation, e.g., Ferrarese & Merritt 2000; Gebhardt et al. 2000), and the dark matter halo mass (Spitler & Forbes 2009). Today, the  $M_*$ - $\sigma_*$  relation is known to have a  $\approx 0.6$  dex scatter and to depend on the galaxy's merger history (Bogdán et al. 2018; Sahu et al. 2019b), and the  $M_*$ - $M_{\text{bulge}}$  relation depends on the morphology of the galaxy (Savorgnan et al. 2016; van den Bosch 2016; Sahu et al. 2019a). Graham (2012), Graham & Scott (2013), Scott et al. (2013), and Davis (2019a) find that there are correlations between  $M_*$  and the luminosity and mass of the bulge, but that the slope is steeper for spiral bulges with a Sérsic profile than for early-type galaxies (ETGs), irrespective of whether the latter are better fitted by a Sérsic or a core-Sérsic profile.

Exciting as these correlations are because of the clues that they may provide regarding galaxy formation and assembly, and about their possible coevolution with the central black hole, they are not without controversy. While Ferrarese (2002), Baes et al. (2003), and Davis et al. (2019b) state that  $M_*$  correlates with the disk maximum rotation velocity and hence with the dark matter halo mass, Kormendy & Bender (2011) retort that black holes do not correlate directly with dark matter haloes, and that a correlation appears only if the galaxy has a bulge. Likewise, Kormendy et al. (2011) contend that black holes do not correlate with either disks or pseudobulges. Davis et al. (2018) argue that  $M_*$  actually correlates with the disk mass, albeit with a low correlation coefficient,  $r = 0.3$ .

Investigating the limits and deviations of these scaling relations, i.e., at high and low masses, may be particularly useful for uncovering the processes that are involved in the formation and evolution of galaxies and their black holes. For example, the  $\log M_*$  versus  $\log M_*$  correlation, with  $M_*$  being the total galaxy stellar mass, has been explored in both ETGs and late-type galaxies (LTGs). Van den Bosch (2016), Davis (2019a), and Sahu et al. (2019a) find that the slope for LTGs is between 70% and 100% steeper than the nearly linear one followed by ETGs. Davis et al. (2019a) rules out that such a steep correlation in LTGs could be due to statistical convergence through hierarchical galaxy formation (Peng 2007; Jahnke & Macciò 2011); in addition, as the LTG in their sample sit on the



Original content from this work may be used under the terms of the [Creative Commons Attribution 4.0 licence](#). Any further distribution of this work must maintain attribution to the author(s) and the title of the work, journal citation and DOI.

**Table 1**  
Observation Log

Galaxy	Filter	$\lambda_{\text{cen}}^{\text{a}}$	FWHM <sup>b</sup>	Exposure s	Camera	Pixel Size arcsec	Program	Date
NGC 3368	$u^*$ (302)	3537 Å	867 Å	5200	Megacam	0.186	18AF99	2018 June 16
	$g'$ (401)	4873 Å	1455 Å	1000	Megacam	0.186	19AF03	2019 March 4
	$i'$ (702)	7776 Å	1508 Å	1600	Megacam	0.186	11AC08	2011 March 1
	$K_s$	2.15 μm	0.33 μm	1660	WIRCam	0.307	17AF12	2017 April 18
	$u^*$ (302)	3537 Å	867 Å	1500	Megacam	0.186	18AF99	2018 June 14
	$g'$ (402)	4720 Å	1520 Å	400	Megacam	0.186	18AF04	2018 May 23
	$i'$ (703)	7764 Å	1554 Å	200	Megacam	0.186	19AF03	2019 April 3
	$K_s$	2.15 μm	0.33 μm	460	WIRCam	0.307	18AF98	2018 July 12
NGC 4395	$u^*$ (302)	3537 Å	867 Å	6900	Megacam	0.186	18AF99	2018 May 23, June 12
	$g'$ (401)	4873 Å	1455 Å	1645	Megacam	0.186	13AS03	2013 February 15
	$r'$ (601)	6282 Å	1219 Å	3304	Megacam	0.186	13AS03	2013 February 13, 15
	$i'$ (702)	7776 Å	1508 Å	1127	Megacam	0.186	13AS03	2013 February 12
	$K_s$	2.15 μm	0.33 μm	760	WIRCam	0.307	17AF12	2017 April 8
	$u^*$ (302)	3537 Å	867 Å	9600	Megacam	0.186	18AF99	2018 May 23, June 13
	$g'$ (401)	4873 Å	1455 Å	2345	Megacam	0.186	19AF03	2019 April 3
	$r'$ (601)	6282 Å	1219 Å	4963	Megacam	0.186	13AS03	2013 February 15, 17; May 3
NGC 4736	$i'$ (702)	7776 Å	1508 Å	1827	Megacam	0.186	11AC08	2011 March 1
	$K_s$	2.15 μm	0.33 μm	880	WIRCam	0.307	13AS03	2013 May 2
	$u^*$ (302)	3537 Å	867 Å	6900	Megacam	0.186	18AF99	2018 May 23, June 12
	$g'$ (401)	4873 Å	1455 Å	1645	Megacam	0.186	19AF03	2019 March 4
	$r'$ (601)	6282 Å	1219 Å	3304	Megacam	0.186	13AS03	2013 February 15
	$i'$ (702)	7776 Å	1508 Å	1127	Megacam	0.186	13AS03	2013 February 12
	$K_s$	2.15 μm	0.33 μm	760	WIRCam	0.307	17AF12	2017 April 8
	$u^*$ (302)	3537 Å	867 Å	9600	Megacam	0.186	18AF99	2018 May 23, June 13

**Notes.**

<sup>a</sup> The central wavelength between the two points defining the FWHM (<http://svo2.cab.inta-csic.es/svo/theory/fps3/index.php?id=CFHT/>).

<sup>b</sup> Ibid.

same correlation, regardless of whether they contain an active galactic nucleus (AGN), they call into question the relevance of AGN feedback to the relation. Reines & Volonteri (2015) analyze two samples, one of ETG and classical bulges, mostly without active AGNs, and another of LTGs with active AGNs. They find similar slopes (1.4 and 1.0, respectively, i.e., less steep for LTGs), but with an offset of more than 1 order of magnitude at  $\log M_*/M_\odot \sim 10$ . In the same parameter space, Simmons et al. (2017) determine that the slope for a sample of AGNs in disk-dominated, merger-free, galaxies is 1.2, roughly equal to that of the bulge sample in Häring & Rix (2004), and with a small offset of  $\sim 0.2$  dex at  $\log M_*/M_\odot = 10$ ; they hence conclude that mergers are inconsequential for the coevolution of black holes and galaxies, and that secular processes, like *calm* accretion and AGN feedback, are more fundamental for galaxy assembly and black hole growth.

An intriguing correlation, given the extremely disparate scales, is the one between the central black hole mass and the total number of GCs ( $N_{\text{GC}}$ ; Burkert & Tremaine 2010; Harris & Harris 2011; Harris et al. 2014). The correlation can be expressed as  $N_{\text{GC}} \propto M_*^{1.02 \pm 0.10}$  and spans over 3 orders of magnitude. Possible causal links have been proposed, for instance, feedback by the jets of AGNs (e.g., Silk & Rees 1998; Fabian 2012) and cannibalization of GCs by black holes (e.g., Capuzzo-Dolcetta & Donnarumma 2001; Capuzzo-Dolcetta & Vicari 2005; Capuzzo-Dolcetta & Mastrobuono-Battisti 2009; Gnedin et al. 2014); as it is roughly linear for ellipticals, it has been argued that it could be due to statistical convergence through merging. On the other hand, GC systems are known to be very good tracers of the galaxy virial mass (e.g., Blakeslee et al. 1997; Spitler & Forbes 2009; Georgiev et al. 2010; Hudson et al. 2014; Harris et al. 2017). This correlation is good

over 7 orders of magnitude in the halo mass, from dwarf galaxies to galaxy clusters, with a strongly declining dispersion with increasing mass,  $\delta N_{\text{GC}}/N_{\text{GC}} \propto M_{\text{vir}}^{1/2}$  (Forbes et al. 2018; Burkert & Forbes 2020).

The study of GC systems in spiral galaxies has been hampered by the sparsity of their GCs, compared to ellipticals, and has been mostly limited to edge-on objects, given the difficulty of detecting individual GCs projected on a spiral disk. Until relatively recently, there were only five spiral galaxies with precise measurements of both  $N_{\text{GC}}$  and  $M_*$ : the Milky Way (MW, Sbc), M104 (Sa), M81 (Sab), M31 (Sb), and NGC 253 (Sc). Burkert & Tremaine (2010) only included the first four, and readily noticed that, while M31, M81, and M104 fall right on the  $N_{\text{GC}} - M_*$  correlation for ellipticals, our Galaxy has a black hole that is about 1 order of magnitude lighter than expected from its  $N_{\text{GC}}$ . They also observed that, compared to M1, M81, and M104, the MW has both a later Hubble type and possibly a pseudobulge, and therefore hypothesized that these factors could be related to its noncompliance with the correlation.

We are in the process of studying the  $N_{\text{GC}}$  versus  $M_*$  correlation in all nine spirals with precise black hole measurements within 16 Mpc: NGC 1068, NGC 3368, NGC 4051, NGC 4151, NGC 4258, NGC 4395, NGC 4736, NGC 4826, and NGC 5055, although so far we only have full data sets for NGC 3368, NGC 4258, NGC 4395, NGC 4736, and NGC 4826. The bulge type was not considered when selecting the sample, but with one exception all of them seem to have a pseudobulge (Kormendy et al. 2010; Kormendy & Ho 2013; Kormendy 2013), while NGC 4258, NGC 4826, and NGC 5055 may also have a classical bulge. The single exception, NGC 4395, is a pure disk, bulgeless, spiral (Filippenko & Ho 2003; Kormendy & Ho 2013). For

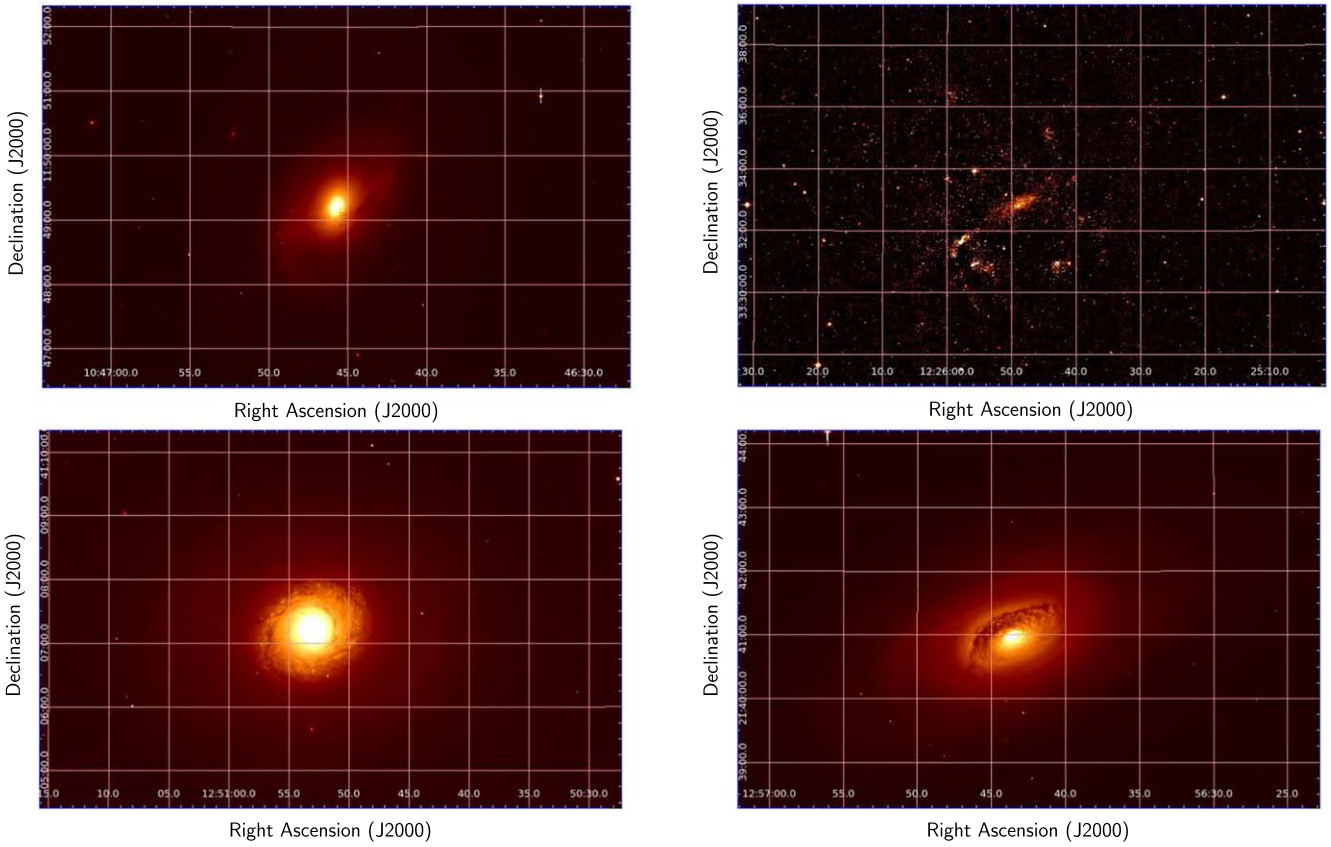


**Figure 1.** CFHT  $i'$ -band images, asinh scale. Top left: NGC 3368; top right: NGC 4395; bottom left: NGC 4736; bottom right: NGC 4826.

**Table 2**  
PSF Star Parameters

Galaxy	Filter	FLUX_RADIUS		MAG_AUTO		N PSF Stars
		Min pixel	Max	Min mag	Max	
NGC 3368	$u^*$	2.10	2.60	16.0	23.0	1998
	$g'$	1.60	2.00	17.5	25.5	3876
	$i'$	1.30	1.60	17.0	23.0	5306
	$K_s$	1.10	1.60	15.5	20.0	1162
NGC 4395	$u^*$	1.80	2.40	17.0	23.0	2379
	$g'$	1.70	2.20	17.0	23.0	3937
	$i'$	1.60	2.10	15.0	21.5	3741
	$K_s$	1.10	1.60	16.0	20.0	449
NGC 4736	$u^*$	2.00	2.70	15.5	22.0	1296
	$g'$	3.10	3.70	16.0	22.9	3112
	$r'$	3.20	3.70	15.5	22.0	4302
	$i'$	2.50	2.80	16.0	22.0	5047
NGC 4826	$K_s$	1.30	1.70	15.0	19.5	320
	$u^*$	2.50	3.10	15.0	23.0	2300
	$g'$	2.00	2.40	16.0	23.0	2379
	$r'$	3.00	3.60	16.0	22.0	5115
	$i'$	1.80	2.20	16.0	22.0	4805
	$K_s$	1.10	1.40	15.5	20.5	519

completeness, we should mention that M31 and M81 have classical bulges, NGC 253 and the MW have pseudobulges, and M104 has both a bulge and a pseudobulge (Kormendy & Ho 2013). Pseudobulges are widely considered the product of secular evolution with few major mergers (e.g., Kormendy & Kennicutt 2004; Athanassoula 2005), although according to, for

example, Sauvaget et al. (2018), they can also be formed by major mergers of gas-rich progenitors in the distant universe.

In this paper, we present new measurements and analyses of the GC systems of the Sab galaxies NGC 3368 (M96), NGC 4736 (M94), and NGC 4826 (M64), and the Sm galaxy NGC 4395. Their surface brightness fluctuation (SBF) distances are  $10.4^{+1.1}_{-1.0}$  Mpc for NGC 3368,  $5.0 \pm 0.4$  Mpc for NGC 4736, and  $7.3 \pm 0.7$  Mpc for NGC 4826 (Tonry et al. 2001; Blakeslee et al. 2010). NGC 4395 is completely devoid of a bulge and hence lacks an SBF measurement; we adopt a Cepheid distance of  $4.3 \pm 0.4$  Mpc (Thim et al. 2004). The masses of their central supermassive black holes are  $(3.6 \pm 1.1) \times 10^5 M_{\odot}$  for NGC 4395 (Peterson et al. 2005);  $(7.5 \pm 1.5) \times 10^6 M_{\odot}$  for NGC 3368;  $6.8^{+1.5}_{-1.6} \times 10^6 M_{\odot}$  for NGC 4736; and  $(1.6 \pm 0.4) \times 10^6 M_{\odot}$  for NGC 4826 (Kormendy & Ho 2013). Their inclinations to the line of sight are  $46.2^\circ$  (NGC 3368),  $33.7^\circ$  (NGC 4395),  $35.6^\circ$  (NGC 4736), and  $57.5^\circ$  (NGC 4826; de Vaucouleurs et al. 1991). We take the following position angles (PA; north to east):  $5^\circ$  (NGC 3368),  $147^\circ$  (NGC 4395), and  $115^\circ$  (NGC 4736 and NGC 4826).

In order to identify globular cluster candidates (GCCs) in these galaxies, we apply the  $(u^* - i')$  versus  $(i' - K_s)$  diagram technique ( $u^*i'K_s$ , hereafter). It is extremely powerful to isolate, in different regions and according to their stellar populations and star formation histories, foreground Galactic stars, background galaxies, young clusters in the disk, and GCCs. In addition, objects in such separate areas of the plot also differ in their light concentration parameters, at least up to a distance of  $\sim 16$  Mpc (Muñoz et al. 2014). The efficacy of the procedure has been corroborated by Powalka et al. (2016) in M87, and by González-Lópezlira et al. (2019), with Optical System for Imaging and

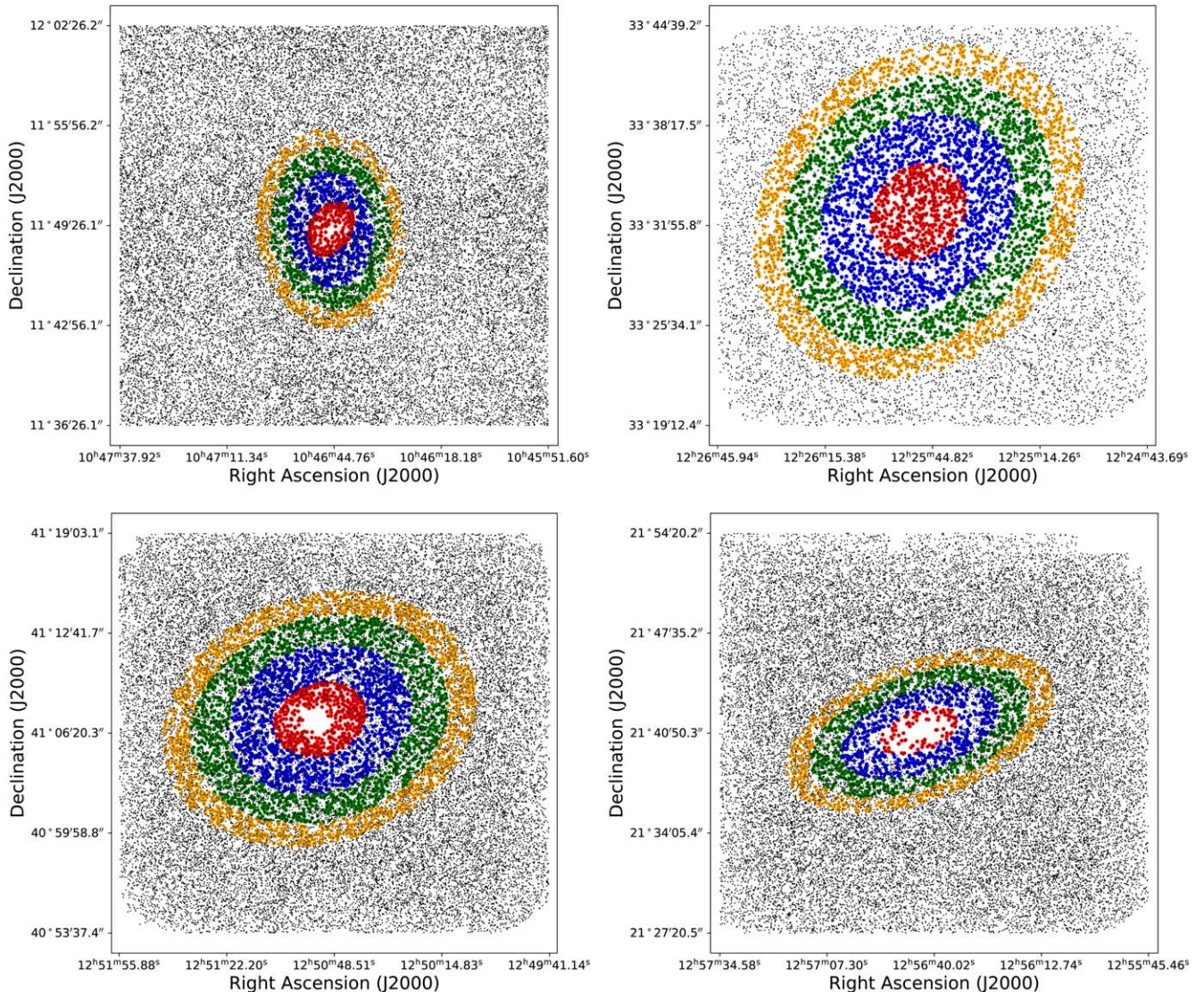


**Figure 2.** Completeness tests, recovered artificial point sources. Top left: NGC 3368; top right: NGC 4395; bottom left: NGC 4736; bottom right: NGC 4826. Colors indicate points from artificial images that were actually used in the fits, to ensure the samples of all regions were statistically equivalent.

low-Intermediate-Resolution Integrated Spectroscopy (OSIRIS) observations of the GC candidates in the megamaser prototype NGC 4258. The method allows for a very low contamination of the samples from foreground stars, background galaxies, and young stellar clusters, even in disk galaxies that are not completely edge-on, and in the absence of radial velocity measurements.

## 2. Data

All the data for this work were obtained with the Canada-France-Hawaii Telescope (CFHT), the optical images with MegaCam (Boulade et al. 2003), and the  $K_s$ -band ones with the Wide-field InfraRed Camera (WIRCam; Puget et al. 2004). MegaCam has a field of view (FOV) of  $0.96 \times 0.94$ , with a plate scale of  $0''.186 \text{ pixel}^{-1}$ , while the FOV of the WIRCam is  $\sim 21' \times 21'$ , with a plate scale of  $0''.307 \text{ pixel}^{-1}$ . Brief descriptions of the detectors’ layouts, cameras’ performances, and data reduction procedures are given in González-Lópezlira et al. (2017). Table 1 provides a summary of the observations.

Except for NGC 4395, the  $g'$ ,  $i'$ , and  $r'$  data are archival, and were originally secured through programs 11AC08 (PI: G. Harris), and 13AS03 (PI: Zhao-Yu Li). The  $u^*$  and  $K_s$ -band images, as well as all the NGC 4395 data, are ours, and were acquired through programs 17AF12, 18AF99 (PI: K. Alamo-Martínez), and 19AF03 (PI: Y. Ordenes-Briceño).

To avoid saturation, individual  $K_s$  exposures of the galaxies were only 10 s long. For NGC 3368, one image was taken in each of the four quadrants of the WIRCam, before nodding the telescope to obtain a sky exposure  $2.5'$  apart. The other three galaxies were observed in an approximately circular pattern with a radius of  $\sim 1.6'$ . Given their large diameters compared to the WIRCam FOV (i.e.,  $R_{25} = 6.6$ ,  $5.6$ , and  $5'$ , respectively, for NGC 4395, NGC 4736, and NGC 4826; de Vaucouleurs et al. 1991), separate (also 10 s long) sky frames were taken, respectively,  $2.5'$  (NGC 4395),  $1.5'$  (NGC 4736) and  $3.5'$  (NGC 4826) away, with the same circular pattern, using the target(T)-sky(S) sequence STTSSTTSS...TTS.

Before combining them into mosaics, the individual optical images were recalibrated with the MegaPipe pipeline (Gwyn 2008), in order to achieve astrometric internal and

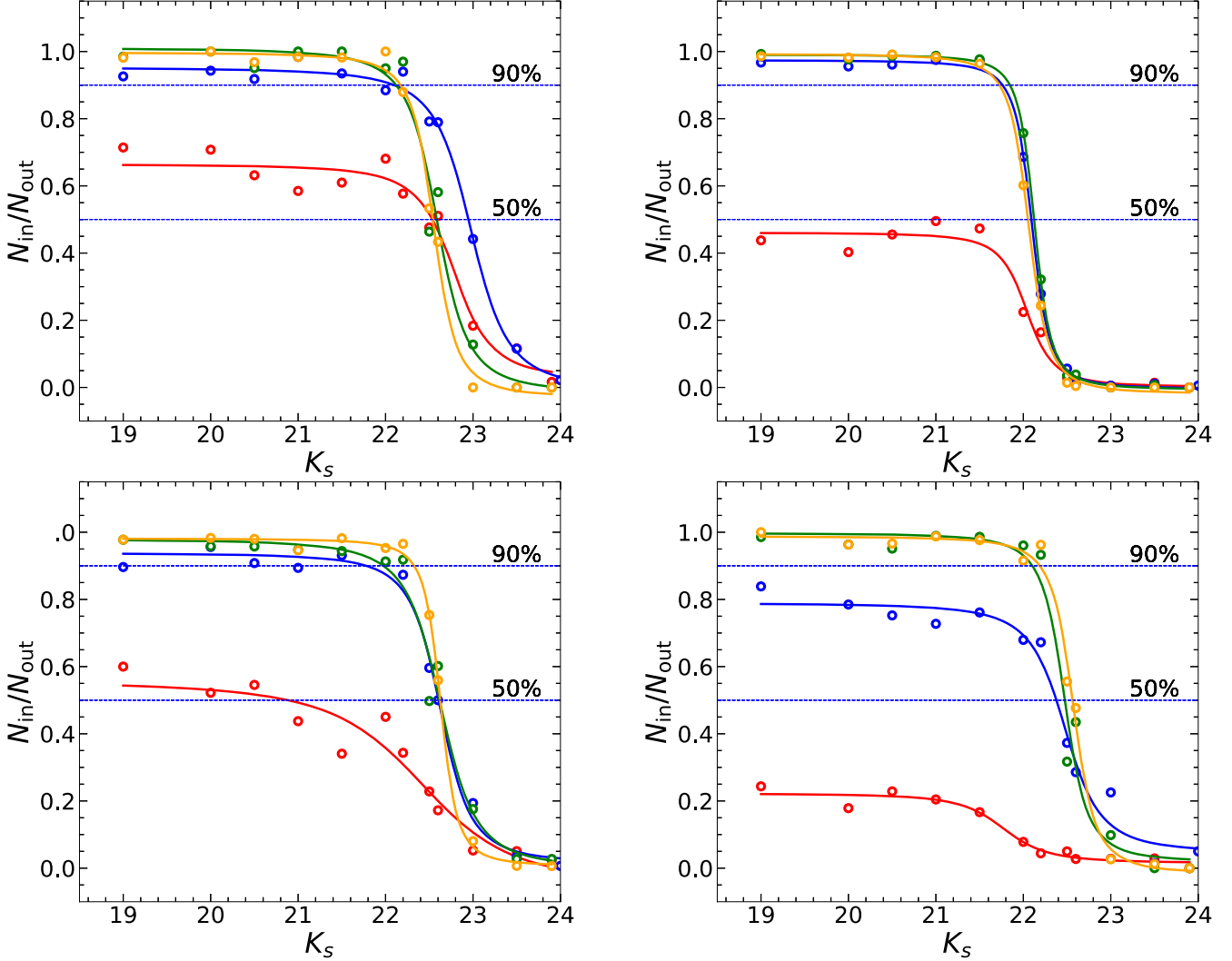


**Figure 3.** Completeness tests. Top left: NGC 3368; top right: NGC 4395; bottom left: NGC 4736; and bottom right: NGC 4826. Fits (solid lines) to recovered fractions (dots) vs.  $K_s$  mag with Equation (2). Colors (red, blue, green, gold) refer to the centermost ellipse, and inner, middle, and external annuli, respectively. Blue dotted lines indicate the 90% and 50% completeness values.

**Table 3**  
Completeness Fit Parameters

Galaxy	Region $R_{25}$	$m_{\text{lim}}$ $K_s$ AB mag	$\alpha_{\text{cutoff}}$	$\gamma$	$\delta$
NGC 3368	0.0–0.5	$22.89 \pm 0.09$	$2.22 \pm 0.71$	$0.69 \pm 0.05$	$0.64 \pm 0.06$
	0.5–1.0	$22.98 \pm 0.03$	$2.24 \pm 0.20$	$0.94 \pm 0.20$	$0.96 \pm 0.20$
	1.0–1.4	$22.69 \pm 0.05$	$2.72 \pm 0.83$	$0.99 \pm 0.83$	$1.03 \pm 0.83$
	1.4–1.7	$22.65 \pm 0.02$	$3.68 \pm 0.66$	$0.97 \pm 0.66$	$1.03 \pm 0.66$
NGC 4395	0.0–0.5	$22.14 \pm 0.05$	$3.09 \pm 1.15$	$0.46 \pm 0.02$	$0.46 \pm 0.03$
	0.5–1.0	$22.10 \pm 0.01$	$4.77 \pm 0.26$	$0.97 \pm 0.26$	$0.98 \pm 0.26$
	1.0–1.4	$22.23 \pm 0.01$	$5.08 \pm 0.23$	$0.98 \pm 0.23$	$1.00 \pm 0.23$
	1.4–1.7	$22.16 \pm 0.01$	$4.26 \pm 0.36$	$0.97 \pm 0.36$	$1.01 \pm 0.36$
NGC 4736	0.0–0.5	$22.52 \pm 0.23$	$0.90 \pm 0.45$	$0.50 \pm 0.08$	$0.62 \pm 0.14$
	0.5–1.0	$22.63 \pm 0.03$	$2.72 \pm 0.32$	$0.95 \pm 0.32$	$0.92 \pm 0.32$
	1.0–1.4	$22.73 \pm 0.05$	$2.36 \pm 0.43$	$0.98 \pm 0.43$	$0.98 \pm 0.43$
	1.4–1.7	$22.73 \pm 0.01$	$5.01 \pm 0.41$	$0.99 \pm 0.41$	$0.98 \pm 0.41$
NGC 4826	0.0–0.5	$21.87 \pm 0.11$	$1.86 \pm 0.65$	$0.24 \pm 0.01$	$0.21 \pm 0.02$
	0.5–1.0	$22.48 \pm 0.05$	$2.33 \pm 0.19$	$0.83 \pm 0.19$	$0.74 \pm 0.19$
	1.0–1.4	$22.57 \pm 0.04$	$3.64 \pm 0.98$	$1.01 \pm 0.98$	$0.98 \pm 0.98$
	1.4–1.7	$22.67 \pm 0.02$	$3.82 \pm 0.68$	$0.97 \pm 0.68$	$1.01 \pm 0.68$

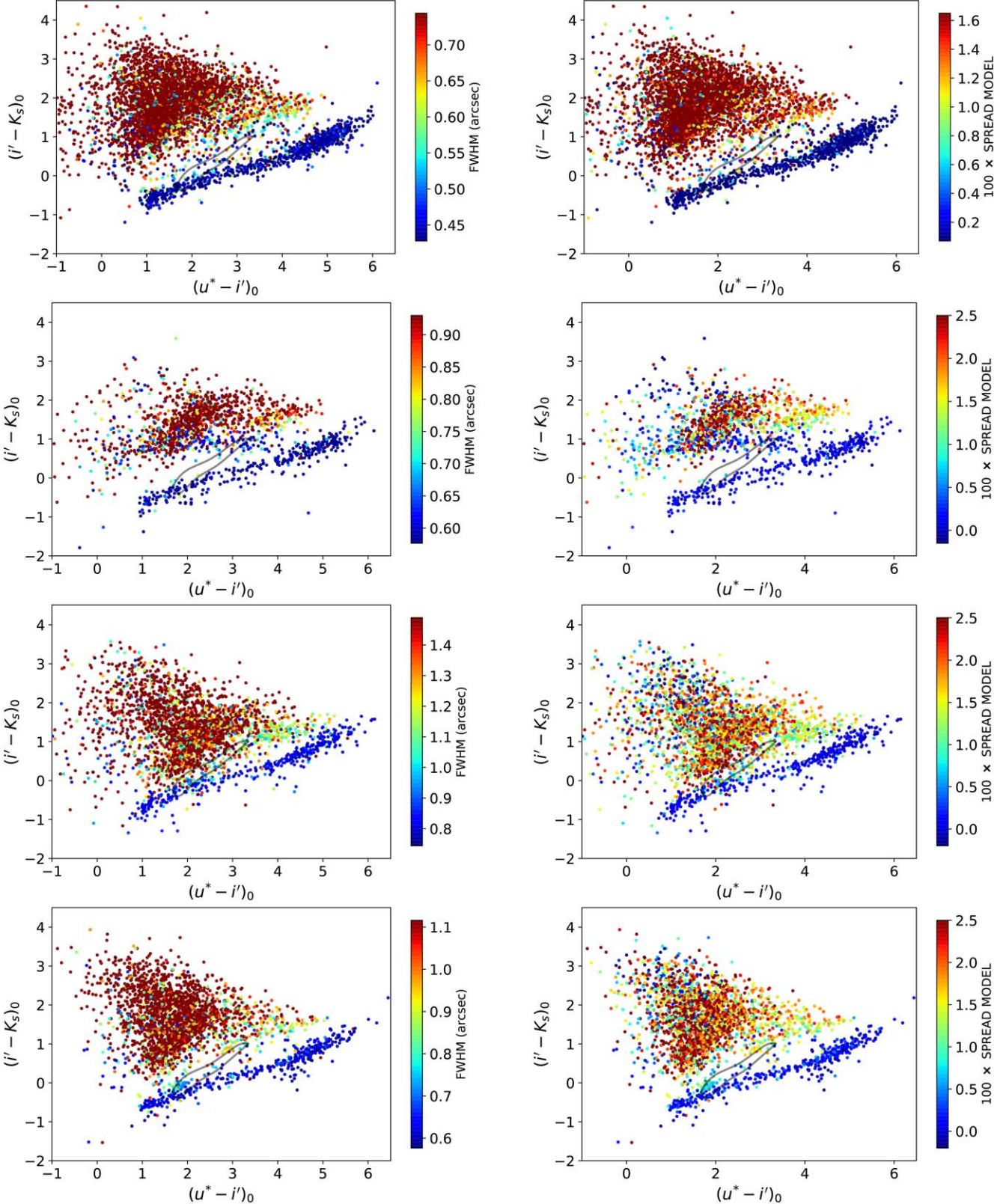


**Figure 4.** Morphology variations across the  $u^*i'K_s$  diagram. Top: NGC 3368; second row: NGC 4395; third row: NGC 4736; bottom: NGC 4826. Indicators of shape in the  $i'$  band are coded as shown by the color bars: FWHM (left) and  $100 \times \text{SPREAD\_MODEL}$  (right).

external accuracies of  $0.^{\prime\prime}04$  and  $0.^{\prime\prime}15$ , respectively, and a photometric accuracy of 0.03 mag. The  $K_s$ -band mosaics were produced with the WIRwolf pipeline (Gwyn 2014), which sky subtracts individual images and achieves an internal astrometric

accuracy of  $0.^{\prime\prime}1$ . Both MegaPipe and WIRwolf render images with photometry in the AB system (Oke 1974), with zero points ( $zp$ ) set to 30 mag. Figure 1 shows images of the four galaxies in the  $i'$  band.

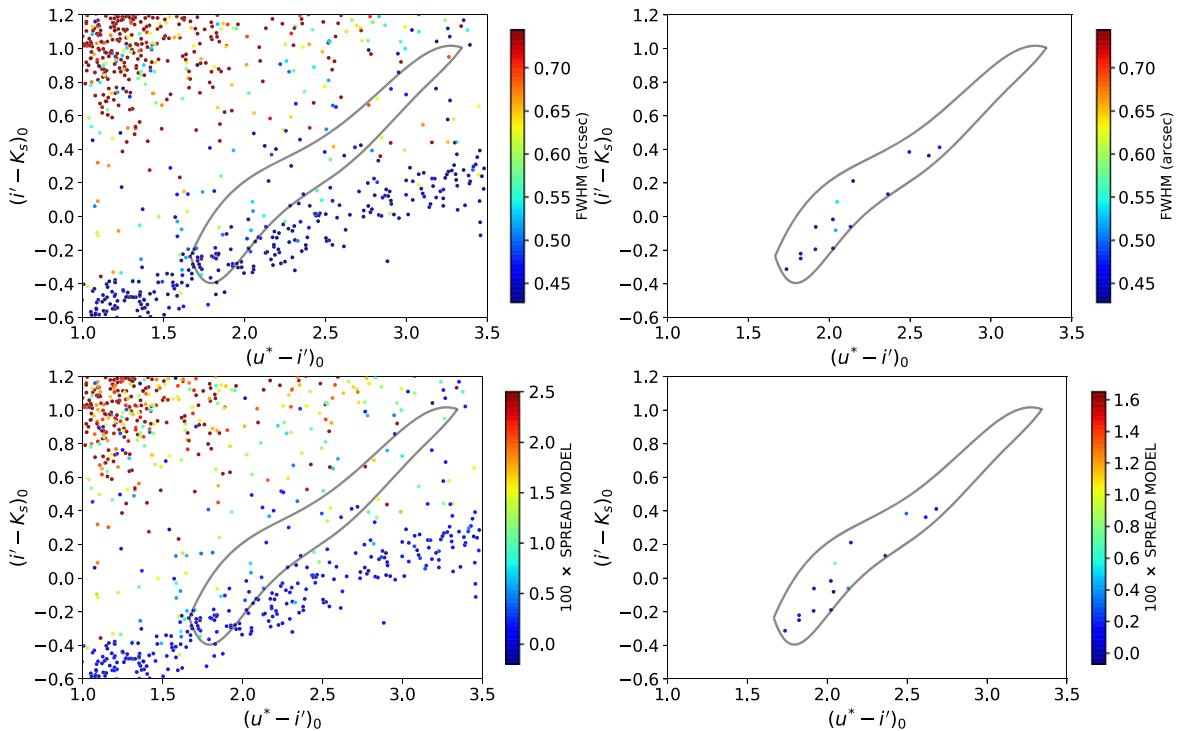


**Figure 5.**  $(u^* - i')$  vs.  $(i' - K_s)_0$  colors and structural parameters of sources in and closely around the selection region of NGC 3368. Top: FWHM; bottom:  $100 \times$  SPREAD\_MODEL. Left column: all sources; right column: final sample. The gray contour outlines the GCC selection region. GCCs appear in shades of blue and cyan in both compactness estimators.

**Table 4**  
Turnover Magnitudes and GCLF Ranges

Filter	$M^0$ mag	NGC 3368		NGC 4395		NGC 4736		NGC 4826	
		$m_{\text{TO}}^0$ mag	$m_{\text{TO}}^0 \pm 3\sigma$ mag						
$u^*$	-5.96	24.12	$20.52 < m_{u^*}^0 < 27.72$	22.21	$19.51 < m_{u^*}^0 < 24.91$	22.53	$18.93 < m_{u^*}^0 < 26.13$	23.36	$20.06 < m_{u^*}^0 < 26.66$
$g'$	-7.20	22.88	$19.28 < m_{g'}^0 < 26.48$	20.97	$18.27 < m_{g'}^0 < 23.67$	21.29	$17.69 < m_{g'}^0 < 24.89$	22.12	$18.82 < m_{g'}^0 < 25.42$
$r'$	-7.69	22.40	$18.80 < m_{r'}^0 < 26.00$	20.48	$17.78 < m_{r'}^0 < 23.18$	20.80	$17.20 < m_{r'}^0 < 24.40$	21.63	$18.33 < m_{r'}^0 < 24.93$
$i'$	-7.92	22.16	$18.56 < m_{i'}^0 < 25.76$	20.25	$17.55 < m_{i'}^0 < 22.95$	20.57	$16.97 < m_{i'}^0 < 24.17$	21.40	$18.10 < m_{i'}^0 < 24.70$
$K_s$	-8.1	22.0	$19.9 < m_{K_s}^0 < 25.6$	20.1	$18.5 < m_{K_s}^0 < 22.8$	20.4	$18.4 < m_{K_s}^0 < 24.0$	21.2	$19.3 < m_{K_s}^0 < 24.5$

### 3. Detection and Photometry

Source detection and photometric measurements in all the stacked images were carried out with SExtractor (Bertin & Arnouts 1996) and PSFEx (Bertin 2011). The detection was performed on images from which their median-filtered version was subtracted; faint sources are detected more easily in a median-subtracted image. All median images were produced with a  $31 \times 31$  pix $^2$  median filter. Conversely, the photometry measurements were made on the original stacked images. PSFEx employs point sources detected in a first pass of SExtractor to build a point-spread function (PSF) model that SExtractor can then apply in a second pass to obtain PSF magnitudes of sources. We chose adequate PSF stars manually, based on their brightness versus compactness, as measured by SExtractor parameters MAG\_AUTO (a Kron-like elliptical aperture magnitude; Kron 1980) and FLUX\_RADIUS (similar to the effective radius); their values for each filter and galaxy are given

in Table 2. A detailed description of this procedure is presented in González-Lópezlira et al. (2017). The spatial variations of the PSF were modeled with polynomials of degree 3. To create the PSF, the flux of each star was measured in an 18 pixel aperture in all bands (equivalent to  $3.^{\prime\prime}3$  in the optical and  $5.^{\prime\prime}5$  at  $K_s$ ); such aperture, determined through the growth-curve method for each passband, is large enough to measure the total flux of the stars, but small enough to reduce the likelihood of contamination by extraneous objects.

### 4. Completeness

Completeness tests were only performed on the  $K_s$ -band mosaics; these are the smallest and shallowest images and, in fact, set our object detection limits. In order to determine the GC detection completeness as a function of the magnitude, 65,000 artificial point sources were generated for each galaxy, based on their respective  $K_s$  PSF model, in the

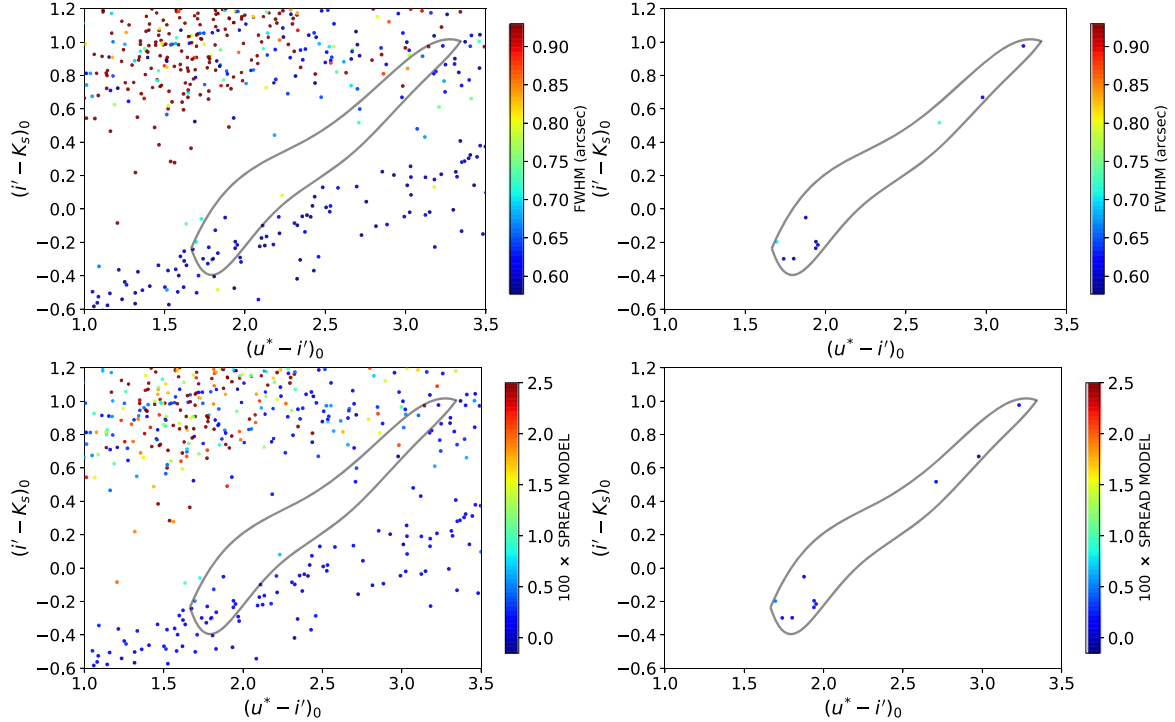


**Figure 6.**  $(u^* - i')$  vs.  $(i' - K_s)$  colors and structural parameters of sources in and closely around the selection region of NGC 4395. Top: FWHM; bottom:  $100 \times$  SPREAD\_MODEL. Left column: all sources; right column: final sample. Symbols as in Figure 5.

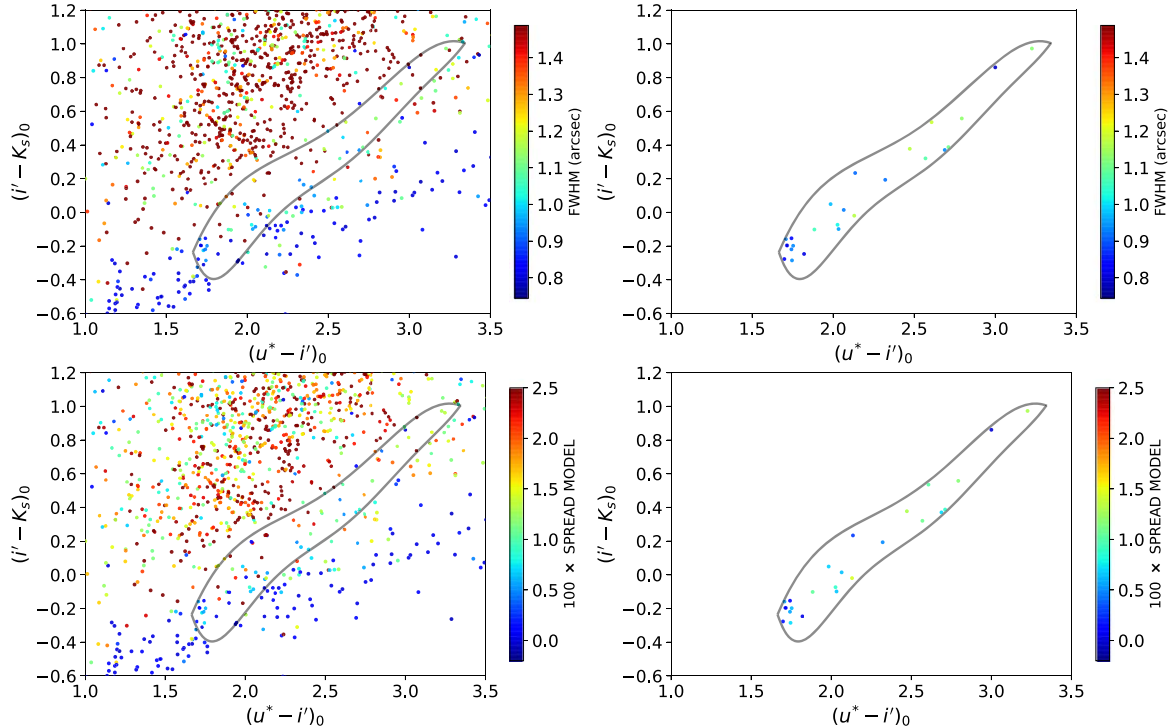


**Figure 7.**  $(u^* - i')$  vs.  $(i' - K_s)$  colors and structural parameters of sources in and closely around the selection region of NGC 4736. Top: FWHM; bottom:  $100 \times$  SPREAD\_MODEL. Left column: all sources; right column: final sample. Symbols as in Figure 5.

interval  $19 \text{ mag} < m_{K_s} < 24 \text{ mag}$ , and with a uniform, or box-shaped, magnitude distribution. Due to the WIRCam pixel size,<sup>8</sup> GCCs are mostly unresolved in the  $K_s$ -band images. The

<sup>8</sup>  $0.''307$  or  $\sim 6 \text{ pc}$ ,  $\gtrsim 7 \text{ pc}$ ,  $\sim 11 \text{ pc}$ , and  $\sim 14.5 \text{ pc}$  at the distances of NGC 4395, NGC 4736, NGC 4826, and NGC 3368, respectively.

artificial objects were only added 500 at a time, to avoid creating artificial crowding; that is, a total of 130 images with simulated sources were produced for each galaxy. The positions of the added sources were random, and assigned without regard to the positions of other artificial objects or real sources.

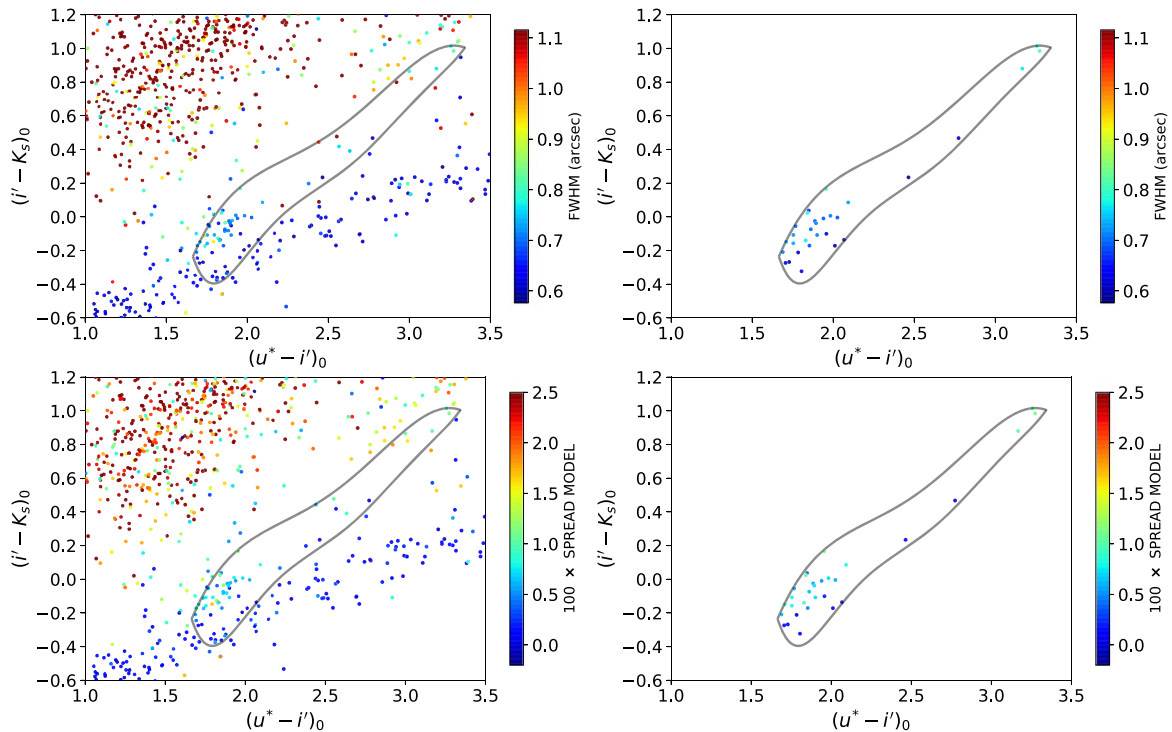


**Figure 8.**  $(u^* - i')$  vs.  $(i' - K_s)$  colors and structural parameters of sources in and closely around the selection region of NGC 4826. Top: FWHM; bottom:  $100 \times$  SPREAD\_MODEL. Left column: all sources; right column: final sample. Symbols as in Figure 5.

Artificial sources were then recovered by running SExtractor on each one of the simulated images, with the same parameters used for the original  $K_s$  galaxy images, and crossmatching the positions of all detections with the known input coordinates of the added objects. Sources with SExtractor output parameter  $\text{FLAGS} \neq 0$  were eliminated; this operation excludes artificial objects falling on top of other artificial or real sources, and hence discards preferentially added objects in crowded regions. The restriction  $\text{FLAGS} = 0$  was also applied in the selection of true sources (see Section 5).

As done previously with NGC 4258 by González-Lópezlira et al. (2017), for all the galaxies we estimated the completeness in four different regions within  $1.7 R_{25}$ : an ellipse with semimajor axis equal to  $0.5 R_{25}$ , and three elliptical annuli from  $0.5$  to  $1.0 R_{25}$ , from  $1.0$  to  $1.4 R_{25}$ , and between  $1.4$  and  $1.7 R_{25}$ . With the exception of the innermost ellipse of NGC 3368, all regions have axis ratios and PA equal to those assumed for the observed disks of the galaxies (respectively, 0.69 and  $5^\circ$  for NGC 3368, 0.82 and  $147^\circ$  for NGC 4395, 0.81 and  $115^\circ$  for NGC 4736, and 0.54 and  $115^\circ$  for NGC 4826); the PA of the central ellipse of NGC 3368 follows the alignment of the surface brightness there, and hence differs from the orientation of the outer isophotes. With the goal of estimating completeness with statistically equivalent samples, for each region we considered a number of added sources inversely proportional to its area; in other words, for the inner ellipses the artificial sources from all 130 images were taken into account, whereas only 43, 34, and 39 were included for the first, second, and third annuli, respectively. On average, for each region we consider  $\sim 2000$  artificial sources in the cases of NGC 4395 and NGC 4736, and  $\sim 1000$  for NGC 3368 and NGC 4826. Figure 2 shows all recovered sources in black, and those from the artificial images actually considered in colors. In the innermost

ellipse (within  $0.5 R_{25}$ ), all recovered sources were used; hence, all dots appear colored in both black and red.

In the case of a box-shaped magnitude distribution, the fraction of recovered artificial sources as a function of magnitude is often well described by the Pritchett function (e.g., McLaughlin et al. 1994):

$$f^P(m) = \frac{1}{2} \left[ 1 - \frac{\alpha_{\text{cutoff}}(m - m_{\text{lim}})}{\sqrt{1 + \alpha_{\text{cutoff}}^2(m - m_{\text{lim}})^2}} \right]; \quad (1)$$

$m_{\text{lim}}$  is the magnitude at which completeness is 50%, and  $\alpha_{\text{cutoff}}$  determines the steepness of the cutoff. However, in the case of crowded regions, where even at bright magnitudes the recovered fraction is flat but  $< 1$ , better fits are obtained with a modified Pritchett function:

$$f^{mP}(m) = \frac{1}{2} \left[ \gamma - \delta \frac{\alpha_{\text{cutoff}}(m - m_{\text{lim}})}{\sqrt{1 + \alpha_{\text{cutoff}}^2(m - m_{\text{lim}})^2}} \right]; \quad (2)$$

here,  $\gamma$  is the asymptotic value of the fraction at bright magnitudes, and  $\delta$  is the fraction at the cutoff.

For each one of the galaxies, the quotient of recovered to added sources as a function of output PSF magnitude was fit with Equation (2), separately for each region. The recovered fractions (dots) and their fits (solid lines) versus  $K_s$  mag are displayed in Figure 3. It is quite obvious that the regions within  $0.5 R_{25}$  are extremely affected by crowding and confusion due to partially resolved sources. This is true also for NGC 4395, in spite of the absence of a conspicuous lack of recovered sources in the central region. The values of the fit parameters  $m_{\text{lim}}$ ,  $\alpha_{\text{cutoff}}$ ,  $\gamma$ , and  $\delta$  are shown in Table 3.

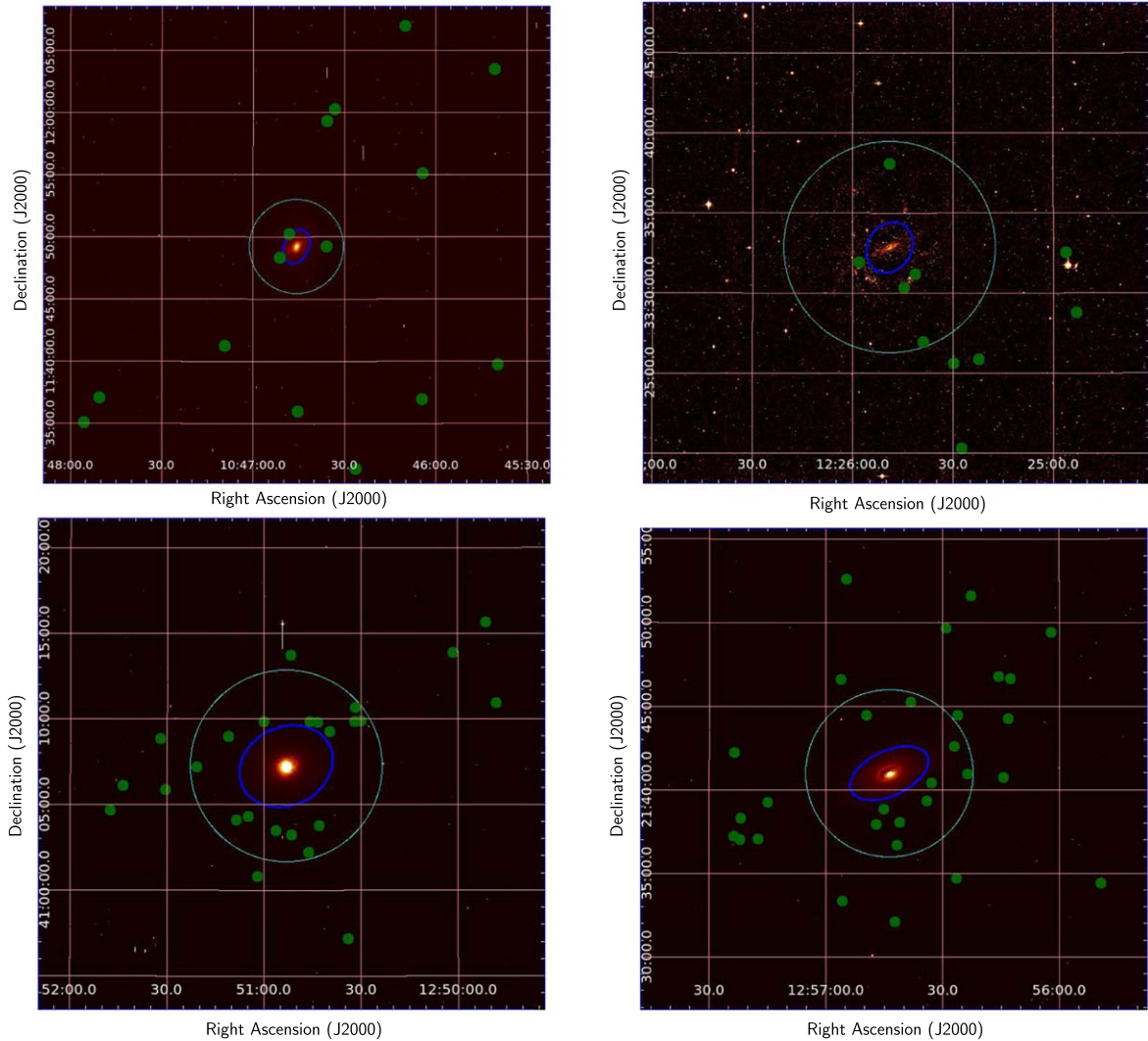


**Figure 9.** Spatial distributions of the GCC samples. Top left: NGC 3368; top right: NGC 4395; bottom left: NGC 4736; bottom right: NGC 4826. The GCCs are shown as *green-filled circles*. Dark blue ellipse: boundary of areas where source confusion is highest (see text); solid cyan line:  $R_{25}$ .

**Table 5**  
*i'*-band Shape Parameters of GCCs in NGC 3368

Name	R.A. J2000 deg	Decl. J2000 deg	100 × (SPREAD _MODEL) $_{i'}$		FWHM $_{i'}$ arcsec	$r_{\text{eff},i'}$ pc	Shape <sup>a</sup>	Index	S/N	$\chi^2$
			0.06	0.42						
J104539+113944	161.4148	11.6624	0.06	0.42	<8.65	KINGx	30	235.8	7.99	
J104540+120330	161.4185	12.0585	0.04	0.42	<9.36	KINGx	100	130.0	4.82	
J104604+115505	161.5179	11.9183	-0.03	0.41	<1.37	KINGx	30	241.4	13.27	
J104604+113655	161.5183	11.6154	0.05	0.42	< 8.01	SERSICx	2	74.8	2.33	
J104609+120658	161.5413	12.1161	-0.04	0.42	<3.44	KINGx	30	104.1	4.63	
J104626+113118	161.6091	11.5219	-0.07	0.41	<3.46	KINGx	30	88.9	3.83	
J104633+120015	161.6379	12.0043	0.02	0.40	< 3.59	SERSICx	2	65.4	2.49	
J104635+115918	161.6478	11.9886	0.10	0.42	<5.19	KINGx	30	86.1	2.20	
J104635+114912	161.6493	11.8201	0.40	0.46	<1.07	KINGx	30	40.4	1.87	
J104645+113554	161.6890	11.5985	-0.07	0.52	< 6.15	SERSICx	2	191.0	10.03	
J104648+115012	161.7003	11.8368	0.30	0.46	<1.68	KINGx	100	61.6	5.50	
J104651+114819	161.7134	11.8053	0.75	0.54	<2.66	KINGx	100	99.6	2.58	
J104709+114112	161.7882	11.6868	-0.00	0.43	< 2.31	SERSICx	2	184.2	7.38	
J104750+113703	161.9601	11.6176	0.01	0.46	<6.00	KINGx	100	36.9	1.83	
J104755+113503	161.9811	11.5844	-0.00	0.45	< 3.46	SERSICx	2	118.2	2.78	

Note. Table 5 is published in its entirety in the machine-readable format. A portion is shown here for guidance regarding its form and content.

<sup>a</sup> Index denotes concentration for King profiles, exponent for Sérsic profiles.

(This table is available in machine-readable form.)

**Table 6**  
*i'*-band Shape Parameters of GCCs in NGC 4395

Name	R.A. J2000 deg	Decl. J2000 deg	100 × (SPREAD)		$r_{\text{eff},i'}$ pc	Shape	Index <sup>a</sup>	S/N	$\chi^2$
			_MODEL) $_{i'}$	FWHM $_{i'}$ arcsec					
J122452+332844	186.2204	33.4792	0.08	0.59	<3.40	KINGx	30	78.2	0.57
J122456+333230	186.2335	33.5418	0.11	0.60	<3.39	SERSICx	2	111.8	0.63
J122522+332549	186.3426	33.4303	0.12	0.59	<2.95	KINGx	100	46.4	0.48
J122527+332015	186.3639	33.3376	0.05	0.59	<3.19	KINGx	100	87.8	0.92
J122529+332536	186.3734	33.4268	0.15	0.60	<2.48	KINGx	100	43.6	0.48
J122538+332654	186.4118	33.4486	0.49	0.70	<6.33	SERSICx	2	28.5	0.45
J122541+333109	186.4210	33.5194	0.16	0.72	<2.86	KINGx	30	19.8	1.00
J122544+333016	186.4354	33.5046	0.16	0.61	<2.99	KINGx	100	15.4	0.50
J122548+333802	186.4535	33.6341	0.14	0.59	<3.09	KINGx	30	26.9	0.57
J122558+333154	186.4917	33.5318	-0.13	0.61	<1.86	KINGx	100	10.1	0.51

**Note.** Table 6 is published in its entirety in the machine-readable format. A portion is shown here for guidance regarding its form and content.

<sup>a</sup> Index denotes concentration for King profiles, exponent for Sérsic profiles.

(This table is available in machine-readable form.)

**Table 7**  
*i'*-band Shape Parameters of GCCs in NGC 4736

Name	R.A. J2000 deg	Decl. J2000 deg	100 × (SPREAD)		$r_{\text{eff},i'}$ pc	Shape	Index <sup>a</sup>	S/N	$\chi^2$
			_MODEL) $_{i'}$	FWHM $_{i'}$ arcsec					
J124947+411056	192.4496	41.1823	1.30	1.13	$8.28^{+0.45}_{-0.19}$	KINGx	30	70.7	0.57
J124951+411538	192.4633	41.2606	0.12	0.81	<1.44	KINGx	100	655.0	2.56
J125001+411350	192.5053	41.2307	0.17	0.83	<3.75	KINGx	100	282.2	1.65
J125029+410951	192.6246	41.1644	0.10	0.84	<3.09	KINGx	100	83.2	0.81
J125031+411039	192.6314	41.1777	0.89	1.10	$5.82^{+0.34}_{-0.33}$	SERSICx	2	44.9	1.06
J125031+410949	192.6329	41.1638	1.03	1.18	$5.74^{+0.45}_{-0.46}$	KINGx	30	29.3	1.04
J125033+405708	192.6415	40.9525	0.04	0.81	<2.89	KINGx	100	325.5	1.53
J125039+410913	192.6651	41.1538	1.05	1.06	$6.69^{+0.16}_{-0.21}$	SERSICx	2	61.0	1.41
J125042+410345	192.6786	41.0625	-0.01	0.79	<4.99	KINGx	30	92.1	0.95
J125043+410947	192.6807	41.1632	0.72	0.94	$3.81^{+0.04}_{-0.09}$	KINGx	100	241.2	1.34
J125045+410950	192.6902	41.1639	0.65	0.93	$2.89^{+0.01}_{-0.12}$	KINGx	100	176.8	1.04
J125046+410210	192.6920	41.0361	0.72	0.94	$3.93^{+0.07}_{-0.02}$	KINGx	100	471.5	2.18
J125051+410314	192.7138	41.0540	0.66	0.96	$2.66^{+0.12}_{-0.06}$	KINGx	100	140.9	0.90
J125051+411341	192.7148	41.2282	0.57	0.93	$2.54^{+0.06}_{-0.03}$	KINGx	100	329.6	1.26
J125056+410327	192.7340	41.0576	1.18	1.13	<7.26	SERSICx	2	58.5	0.73
J125059+410949	192.7500	41.1637	1.44	1.17	$13.05^{+0.51}_{-0.30}$	KINGx	100	147.9	1.03
J125101+410046	192.7577	41.0128	0.29	0.91	$1.33^{+0.41}_{-0.41}$	KINGx	30	44.4	0.88
J125104+410416	192.7698	41.0712	0.50	0.92	$3.27^{+0.07}_{-0.08}$	SERSICx	2	163.1	1.18
J125108+410404	192.7848	41.0679	0.69	0.97	$3.00^{+0.35}_{-0.23}$	KINGx	30	36.7	0.77
J125110+410856	192.7957	41.1491	0.63	0.94	$3.87^{+0.05}_{-0.09}$	KINGx	30	229.6	1.26
J125120+410710	192.8362	41.1197	1.32	1.17	$8.97^{+0.48}_{-0.18}$	SERSICx	2	93.6	1.03
J125130+410551	192.8767	41.0977	0.03	0.84	<3.24	KINGx	100	90.5	1.05
J125131+410849	192.8828	41.1472	0.58	0.93	$2.42^{+0.02}_{-0.01}$	KINGx	100	608.9	1.83
J125143+410606	192.9315	41.1018	0.90	1.02	$5.08^{+0.22}_{-0.12}$	KINGx	100	192.4	0.96
J125147+410439	192.9478	41.0776	1.09	1.08	$8.08^{+0.19}_{-0.38}$	KINGx	100	147.0	0.86

**Note.** Table 7 is published in its entirety in the machine-readable format. A portion is shown here for guidance regarding its form and content.

<sup>a</sup> Index denotes concentration for King profiles, exponent for Sérsic profiles.

(This table is available in machine-readable form.)

## 5. Selection of GCCs

The main tool used for the selection of GCCs is the ( $u^* - i'$ ) versus ( $i' - K_s$ ) color–color diagram (Muñoz et al. 2014). The combination of optical and near-infrared data in this parameter space constitutes the most powerful photometric-only method for the selection of a clean sample of GC candidates. It probes

simultaneously the main-sequence turnoff, and the red giant and horizontal branches of stellar populations. In this plane, GCs occupy a region that is distinct from the areas inhabited by background galaxies, on the one hand, and foreground Galactic stars, on the other. Objects in these various regions not only have different stellar populations, but light concentration parameters that roughly distinguish GCs, which appear

**Table 8**  
*i'*-band Shape Parameters of GCCs in NGC 4826

Name	R.A. J2000 deg	Decl. J2000 deg	100 × (SPREAD _MODEL) <i>i'</i>	FWHM <sub><i>i'</i></sub> arcsec	<i>r</i> <sub>eff,<i>i'</i></sub> pc	Shape	Index <sup>a</sup>	S/N	$\chi^2$
J125549+213423	193.9550	21.5733	0.12	0.61	<2.42	KINGx	30	296.5	4.55
J125601+214923	194.0083	21.8233	0.48	0.69	2.81 <sub>-0.07</sub> <sup>+0.11</sup>	SERSICx	2	136.4	2.30
J125612+214638	194.0522	21.7773	0.12	0.58	<4.72	KINGx	100	34.1	1.04
J125613+214412	194.0544	21.7368	1.13	0.82	9.45 <sub>-0.22</sub> <sup>+0.13</sup>	KINGx	30	131.5	1.28
J125614+214043	194.0592	21.6789	0.73	0.71	4.04 <sub>-0.13</sub> <sup>+0.07</sup>	KINGx	100	136.5	1.44
J125615+214645	194.0648	21.7794	0.20	0.62	<4.62	KINGx	100	119.5	1.86
J125622+215134	194.0944	21.8597	0.15	0.61	<2.01	KINGx	100	114.8	1.44
J125623+214054	194.0982	21.6817	1.10	0.78	7.21 <sub>-0.09</sub> <sup>+0.09</sup>	KINGx	30	188.4	2.36
J125625+214427	194.1082	21.7408	0.72	0.71	3.37 <sub>-0.03</sub> <sup>+0.08</sup>	KINGx	100	203.9	1.82
J125626+213440	194.1095	21.5779	0.10	0.62	<1.28	KINGx	30	137.0	1.33
J125626+214234	194.1124	21.7096	0.71	0.71	3.71 <sub>-0.05</sub> <sup>+0.12</sup>	KINGx	100	173.8	2.65
J125628+214937	194.1207	21.8272	1.15	0.81	8.80 <sub>-0.01</sub> <sup>+0.07</sup>	SERSICx	2	262.1	5.35
J125632+214023	194.1364	21.6733	0.43	0.67	1.85 <sub>-0.08</sub> <sup>+0.07</sup>	KINGx	100	80.2	2.13
J125633+213919	194.1416	21.6554	0.84	0.74	4.88 <sub>-0.10</sub> <sup>+0.10</sup>	KINGx	100	182.8	1.13
J125638+214512	194.1583	21.7535	0.01	0.60	<5.98	KINGx	100	32.3	0.76
J125641+213802	194.1709	21.6341	0.64	0.70	3.90 <sub>-0.09</sub> <sup>+0.16</sup>	KINGx	30	82.2	0.86
J125641+213641	194.1734	21.6115	0.58	0.69	2.86 <sub>-0.02</sub> <sup>+0.10</sup>	KINGx	100	159.9	1.20
J125642+213204	194.1761	21.5347	0.52	0.69	2.53 <sub>-0.07</sub> <sup>+0.10</sup>	KINGx	100	109.9	1.00
J125644+213848	194.1873	21.6468	0.79	0.73	4.38 <sub>-0.05</sub> <sup>+0.14</sup>	KINGx	100	185.4	2.14
J125646+213754	194.1954	21.6317	0.55	0.69	2.70 <sub>-0.07</sub> <sup>+0.18</sup>	KINGx	100	82.2	1.01
J125649+214425	194.2065	21.7404	0.81	0.73	4.88 <sub>-0.12</sub> <sup>+0.07</sup>	KINGx	100	151.2	1.52
J125654+215233	194.2275	21.8760	1.04	0.77	8.76 <sub>-0.30</sub> <sup>+0.34</sup>	KINGx	100	109.5	1.16
J125655+213319	194.2323	21.5554	0.05	0.60	<5.97	KINGx	30	64.2	1.07
J125655+214633	194.2332	21.7761	0.97	0.77	6.74 <sub>-0.15</sub> <sup>+0.20</sup>	KINGx	100	151.3	1.02
J125714+213914	194.3117	21.6540	0.13	0.62	<1.44	KINGx	30	256.8	3.05
J125717+213702	194.3225	21.6173	0.56	0.69	3.60 <sub>-0.17</sub> <sup>+0.12</sup>	KINGx	30	79.0	0.87
J125721+213816	194.3410	21.6378	0.98	0.78	7.40 <sub>-0.18</sub> <sup>+0.18</sup>	KINGx	30	87.3	0.87
J125722+213659	194.3418	21.6166	0.03	0.61	<1.14	KINGx	30	208.9	2.46
J125723+214212	194.3472	21.7036	0.62	0.71	3.37 <sub>-0.07</sub> <sup>+0.12</sup>	KINGx	100	134.4	1.64
J125723+213711	194.3480	21.6198	0.80	0.74	4.72 <sub>-0.10</sub> <sup>+0.14</sup>	KINGx	100	160.6	1.27

**Note.** Table 8 is published in its entirety in the machine-readable format. A portion is shown here for guidance regarding its form and content.

<sup>a</sup> Index denotes concentration for King profiles, exponent for Sérsic profiles.

(This table is available in machine-readable form.)

marginally resolved in the optical, from both point and extended sources.

Figure 4 shows the  $u^*i'K_s$  diagrams for all the sources detected in the images of NGC 3368 (top row), NGC 4395 (second row), NGC 4736 (third row), and NGC 4826 (bottom row). All the data have been corrected for Galactic extinction, using the values from Schlafly & Finkbeiner (2011) given for the Sloan Digital Sky Survey filters by the NASA Extragalactic Database,<sup>9</sup> respectively, for NGC 3368,  $A_u = 0.107$ ,  $A_g = 0.083$ ,  $A_i = 0.043$ ,  $A_{K_s} = 0.005$ ; for NGC 4395,  $A_u = 0.073$ ,  $A_g = 0.057$ ,  $A_i = 0.029$ ,  $A_{K_s} = 0.008$ ; for NGC 4736,  $A_u = 0.075$ ,  $A_g = 0.059$ ,  $A_r = 0.041$ ,  $A_i = 0.030$ ,  $A_{K_s} = 0.005$ ; and for NGC 4826,  $A_u = 0.175$ ,  $A_g = 0.137$ ,  $A_r = 0.095$ ,  $A_i = 0.070$ ,  $A_{K_s} = 0.012$ .

The sources are color coded by their light concentration in the *i'* band, as gauged by the FWHM (left column), and 100× the dimensionless SExtractor parameter SPREAD\_MODEL (right column).<sup>10</sup> In these panels, reddish-brown sources are extended, blue sources are pointlike, and cyan sources are marginally

resolved. The color limits have been chosen to highlight these differences. Objects in the reddish-brown cloud are mostly galaxies, while those in the blue band are main-sequence stars in our Galaxy.

In between the galaxy cloud and the stellar band, the selection region for GCCs is indicated by the gray contour. The selection region was determined using data from the giant elliptical M87 (Muñoz et al. 2014; Powalka et al. 2016); it has the shape of a drop or pennon, and contains more than 2000 spectroscopically confirmed GCs in that galaxy. The technique has already been applied to the spiral megamaser prototype NGC 4258 (González-Lópezlira et al. 2017), and its effectiveness in spirals assessed by González-Lópezlira et al. (2019). One difference with the observations of M87 and our previous work on NGC 4258 is that a new  $u^*$  filter was used for the observations presented in this paper. As a consequence, the  $u^*$  luminosity function turnover (LFTO) is slightly fainter, and the GC selection region shifted 0.24 mag to the red in ( $u^* - i'$ ).

The spectroscopic observations of the NGC 4258 GCCs reported by González-Lópezlira et al. (2019) found no false negatives, and a sample contamination of, conservatively, 7/23 or 30%, fully consistent with the 50–100 contaminants found by Powalka et al. (2016) for the GCCs of M87, in a FOV 9 times larger. Like M87 and NGC 4258, the fields of NGC 3368, NGC 4395, NGC 4736, and NGC 4826 lie at high Galactic

<sup>9</sup> The NASA/IPA Extragalactic Database (NED) is operated by the Jet Propulsion Laboratory, California Institute of Technology, under contract with the National Aeronautics and Space Administration.

<sup>10</sup> For each object, the SPREAD\_MODEL value results from the comparison between its best-fitting PSF, and the convolution of such PSF with an exponential disk whose scale length is equal to the FWHM of said PSF (Desai et al. 2012).

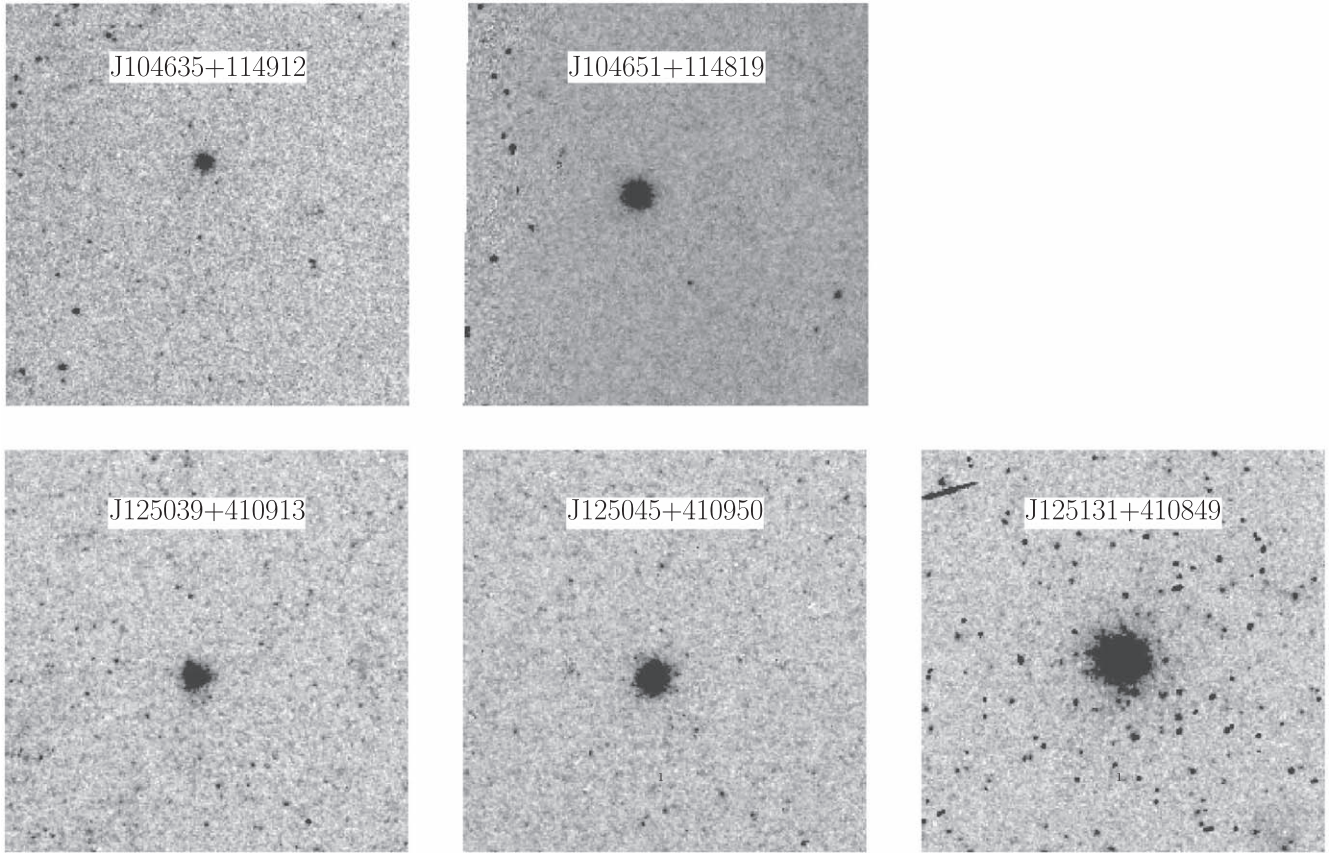


**Figure 10.** Grayscale images of GC candidates, from HST exposures. Top, left to right: J104635+114912 and J104651+114819, in NGC 3368. Bottom: J125039+410913, J125045+410950, and J125131+410849, in NGC 4736.

latitudes of  $b = 57^{\circ}0$ ,  $b = 81^{\circ}5$ ,  $b = 76^{\circ}0$ , and  $b = 84^{\circ}4$ , respectively.

González-Lópezlira et al. (2019) also determined that the contaminants could be reduced by setting the light concentration parameters SPREAD\_MODEL  $\leq 0.015$  and FWHM  $\leq 29$  pc ( $0.^{\prime\prime}58$  for NGC 3368,  $1.^{\prime\prime}40$  for NGC 4395,  $1.^{\prime\prime}20$  for NGC 4736, and  $0.^{\prime\prime}82$  for NGC 4826). Moreover, we only kept objects within  $\pm 3\sigma$  of the expected GC LFTO magnitude in every filter, except at  $K_s$ , as González-Lópezlira et al. (2019) realized that objects more than  $1.7 \times \sigma$  brighter than the turnoff at that wavelength were potential contaminants. Other restrictions were an axis ratio  $\geq 0.7$  and an error MAGERR\_PSF  $< 0.2$  mag, both in the  $i'$  band, as well as FLAGS = 0 in all bands. The standard deviation of the GCLF depends on the galaxy luminosity (Jordán et al. 2007); based on their Equation (18), we have assumed 0.9 for NGC 4395, 1.1 for NGC 4826, and 1.2 for NGC 3368 and NGC 4736.<sup>11</sup> Values of the LFTO in the optical were derived by combining the absolute LFTO magnitude in the  $g$  band,  $M_g^0 = -7.2$  mag (Jordán et al. 2007), with the (AB) colors given in the MegaCam filter system by (Bruzual & Charlot 2003) models for an SSP with  $Z = 0.0004$ , an age of 12 Gyr, and a Chabrier initial mass function (IMF; Chabrier 2003). The LFTO in the  $V$  band would be  $M_V^0 = -7.4$  mag. The LFTO magnitude in the  $K_s$  band was taken from Wang et al. (2014). The TO absolute magnitudes, observed LFTO magnitudes, and magnitude ranges of the GCLF are shown in Table 4.

<sup>11</sup> The MW GCLF has  $\sigma_V = 1.15 \pm 0.1$  (Jordán et al. 2007), also consistent with their Equation (18).

Figures 5–8 (left column) show the  $u^*i'K_s$  diagram, FWHM (top rows), and  $100 \times$  structural parameter SPREAD\_MODEL (bottom rows) of sources in and closely around the GCC selection region (gray contour) for NGC 3368, NGC 4395, NGC 4736, and NGC 4826, respectively. The GCC final samples for the galaxies are displayed in the right column.

The spatial distributions of the GCC samples are shown in Figure 9. The members of the samples are displayed as green circles on the  $i'$ -band images of NGC 3368 (top left), NGC 4395 (top right), NGC 4736 (bottom left), and NGC 4826 (bottom right). The dark blue ellipses outline the regions where source confusion is highest, inferred from the completeness simulations and the dearth of GCC detections. This boundary is located at  $0.375 R_{25}$  for NGC 3368,  $0.25 R_{25}$  for NGC 4395, and  $0.5 R_{25}$  for both NGC 4736 and NGC 4826. The cyan circles indicate  $R_{25}$ .

Given the distances to the galaxies, as well as the resolution of the MegaCam data (1 MegaCam pixel =  $0.^{\prime\prime}186$ ; i.e.,  $\simeq 3.9$ , 4.5, 6.6, and 9.4 pc, respectively, for NGC 4395, NGC 4736, NGC 4826, and NGC 3368), we have also been able to calculate the half-light radii,  $r_e$ , in the  $i'$  band of all the candidates. To this end, we used the program ISHAPE (Larsen 1999) in the BAOLAB<sup>12</sup> software package. ISHAPE measures the size of a compact source by comparing its observed light profile with models generated by convolving different analytical profiles with the image PSF. For data with a signal-to-noise ratio (S/N)  $\gtrsim 30$ , ISHAPE can measure  $r_{\text{eff}}$  reliably down to  $\sim 0.1$  the PSF FWHM, or  $\sim 1.7$  pc for

<sup>12</sup> <http://baolab.astroduo.org>

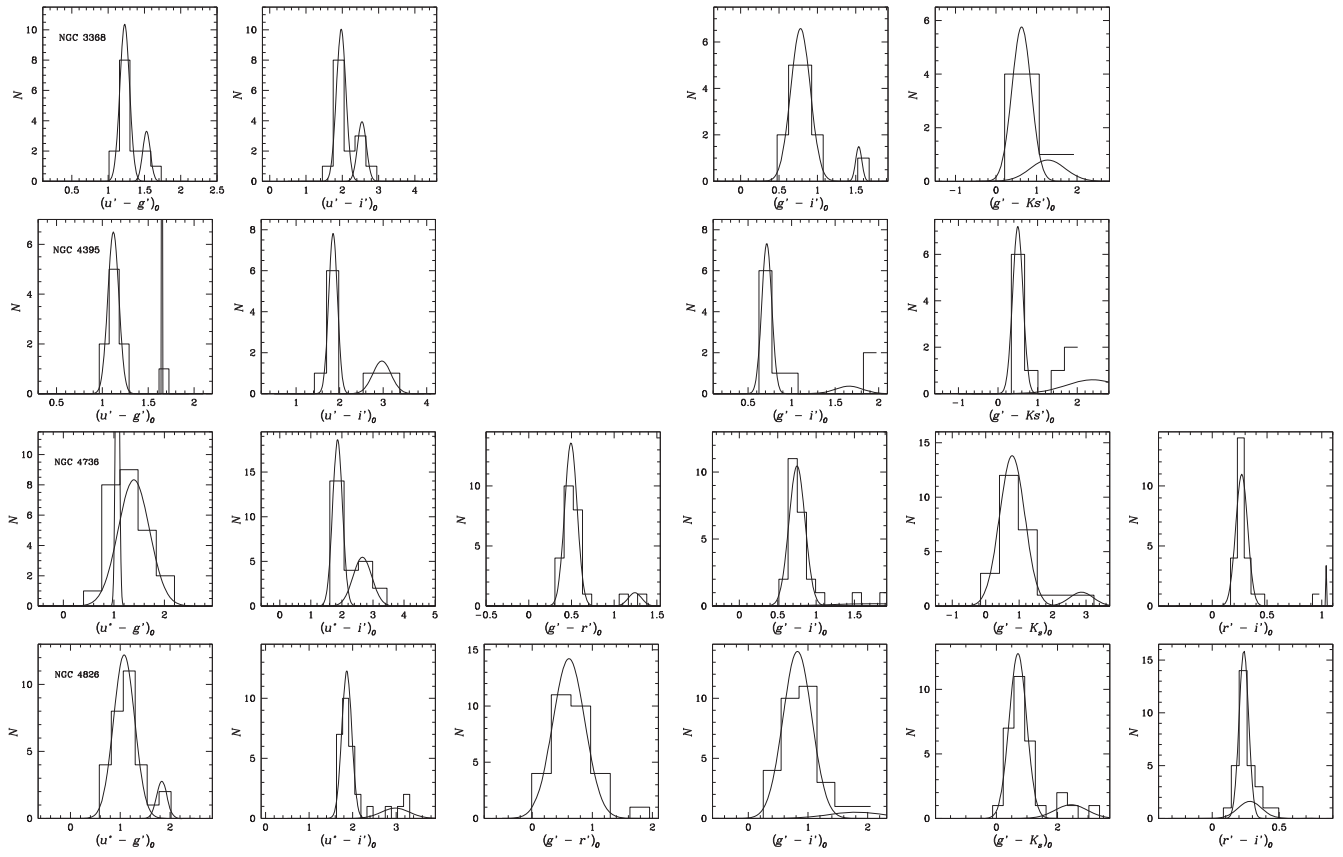


**Figure 11.** Color distributions of GC systems. Top: NGC 3368 GCCs; second row: NGC 4395; third row: NGC 4736; bottom: NGC 4826. From left to right:  $(u^* - g')$ ,  $(u^* - i')$ ,  $(g' - r')$ ,  $(g' - K_s)$ ,  $(r' - i')$ .

NGC 4736, 2.3 pc for NGC 4826, 2.4 pc for NGC 3368, and 2.5 pc for NGC 4395; objects smaller than this are effectively unresolved (Larsen 1999; Harris et al. 2009). We fitted all the sources with King (King 1962, 1966) and Sérsic (Sérsic 1963) profiles. For King profiles, we tried fixed concentration indices ( $C \equiv r_{\text{tidal}}/r_{\text{core}}$ ) of 30 and 100; in the case of Sérsic, we chose a fixed exponent of 2.<sup>13</sup> For each object, the model providing the fit to the data with the smallest  $\chi^2$  residuals was then used to derive the effective radius, by applying the conversion factors between  $r_{\text{eff}}$  and FWHM given in the ISHAPE manual. For each galaxy, Tables 5–8 list shape parameters in the  $i'$  band: FWHM,  $100 \times \text{SPREAD\_MODEL}$ ,  $r_e$ , the type and index of the best-fitting profile, the S/N of the data, and the  $\chi^2$  of the fit.

We present in Figure 10 a few exposures of GCCs in NGC 3368 and NGC 4736 that we were able to find in the Hubble Space Telescope (HST) Legacy Archive; their visual appearance is consistent with their classification. J104635+114912 was identified in the Advance Camera for Surveys (ACS) frame hst\_10433\_02\_acs\_wfc\_f555w.fits (filter F555W, proposal GO 10433, PI: B. Madore); J104651+114819, in the Wide Field Camera 3 (WFC3) image hst\_13364\_07\_wfc3\_u-vis\_f555w.fits (F555W, proposal GO 13364, PI: D. Calzetti). All the NGC 4736 images were acquired with the ACS. J125039+410913 and J125045+410950 were identified in the frame hst\_10402\_09\_acs\_wfc\_f555w\_drz.fits (proposal GO 10402, PI: R. Chandar); J125131+410849, in hst\_9480\_u8\_

acs\_wfc\_f775w\_drz.fits (filter F775W, proposal GO/PAR 9480, PI: J. Rhodes).

## 6. Properties of the GC Systems

### 6.1. Color Distribution

The distributions of our final samples of GCCs in the colors  $(u^* - g')$ ,  $(u^* - i')$ ,  $(g' - r')$ ,  $(g' - i')$ ,  $(r' - i')$ , and  $(g' - K_s)$ , fit with two heteroscedastic Gaussians, are shown in Figure 11. The colors of the individual candidates, shown in Tables 9–12, have been corrected for foreground extinction in the MW, as already mentioned. The means and dispersions of the Gaussian fits are presented in Table 13.

González-Lópezlira et al. (2017) found that the colors of GCs and GCCs in the MW, M31 and NGC 4258 were remarkably consistent, once internal extinction was taken into account. The same is true for NGC 3368, NGC 4395, NGC 4736, and NGC 4826. Their GCC colors have not been corrected for internal extinction, and the bluer Gaussians fit to their color distributions are bracketed by the values of single Gaussian fits to the GC system of M31, with and without such correction. Both these and the colors of the MW GC system are shown in Table 14.

### 6.2. Luminosity Functions

The  $K_s$ -band luminosity functions of the final samples of GCCs of the four galaxies are shown in Figure 12. Given the exclusion of the regions close to the centers of the galaxies, i.e., the areas most affected by crowding and confusion, the corrections for incompleteness would be barely significant. The

<sup>13</sup> According to Turner et al. (2012), based on the measurements of Graham & Spitler (2009) and Seth et al. (2010), a Sérsic parameter of  $\sim 2$  represents Galactic GCs and nuclear clusters well.

**Table 9**  
Colors of GCCs in NGC 3368

Name	R.A. J2000 deg	Decl. J2000 deg	$g'_0$ mag	$\Delta g'_0$ mag	$K_{s,0}$ mag	$\Delta K_{s,0}$ mag	$(u^* - i')_0$ mag	$\Delta (u^* - i')_0$ mag	$(g' - i')_0$ mag	$\Delta (g' - i')_0$ mag	$(i' - K_s)_0$ mag	$\Delta (i' - K_s)_0$ mag
J104539+113944	161.4148	11.6624	20.493	0.002	19.97	0.03	1.824	0.005	0.668	0.003	-0.22	0.03
J104540+120330	161.4185	12.0585	21.092	0.003	20.76	0.08	1.736	0.008	0.566	0.004	-0.31	0.08
J104604+115505	161.5179	11.9183	20.401	0.002	19.97	0.03	1.823	0.005	0.602	0.003	-0.25	0.03
J104604+113655	161.5183	11.6154	21.950	0.006	20.85	0.08	2.148	0.018	0.811	0.007	0.21	0.08
J104609+120658	161.5413	12.1161	21.510	0.004	20.89	0.10	2.023	0.010	0.736	0.005	-0.19	0.10
J104626+113118	161.6091	11.5219	21.837	0.005	20.73	0.13	2.363	0.014	0.900	0.006	0.13	0.13
J104633+120015	161.6379	12.0043	22.081	0.007	21.28	0.15	1.917	0.015	0.787	0.008	-0.06	0.15
J104635+115918	161.6478	11.9886	22.025	0.006	20.56	0.04	2.616	0.020	1.026	0.006	0.36	0.04
J104635+114912	161.6493	11.8201	22.666	0.011	21.77	0.10	2.132	0.028	0.880	0.012	-0.06	0.10
J104645+113554	161.6890	11.5985	20.774	0.002	20.07	0.02	2.040	0.007	0.714	0.003	-0.08	0.02
J104648+115012	161.7003	11.8368	22.118	0.006	20.70	0.03	2.495	0.021	0.963	0.007	0.38	0.03
J104651+114819	161.7134	11.8053	21.527	0.004	20.54	0.02	2.049	0.011	0.828	0.005	0.09	0.02
J104709+114112	161.7882	11.6868	20.870	0.003	20.05	0.04	2.023	0.006	0.759	0.003	-0.02	0.04
J104750+113703	161.9601	11.6176	23.451	0.018	21.43	0.11	2.682	0.045	1.539	0.019	0.41	0.11
J104755+113503	161.9811	11.5844	21.309	0.004	20.74	0.06	1.914	0.010	0.687	0.005	-0.19	0.06

(This table is available in machine-readable form.)

**Table 10**  
Colors of GCCs in NGC 4395

Name	R.A. J2000 deg	Decl. J2000 deg	$g'_0$ mag	$\Delta g'_0$ mag	$K_{s,0}$ mag	$\Delta K_{s,0}$ mag	$(u^* - i')_0$ mag	$\Delta (u^* - i')_0$ mag	$(g' - i')_0$ mag	$\Delta (g' - i')_0$ mag	$(i' - K_s)_0$ mag	$\Delta (i' - K_s)_0$ mag
J122452+332844	186.2204	33.4792	20.001	0.004	19.59	0.03	1.802	0.007	0.656	0.006	-0.30	0.03
J122456+333230	186.2335	33.5418	19.580	0.003	19.17	0.02	1.739	0.005	0.654	0.004	-0.30	0.02
J122522+332549	186.3426	33.4303	20.697	0.006	20.08	0.04	1.940	0.012	0.761	0.009	-0.20	0.04
J122527+332015	186.3639	33.3376	20.041	0.004	19.23	0.03	1.877	0.008	0.813	0.005	-0.05	0.03
J122529+332536	186.3734	33.4268	20.734	0.007	20.17	0.04	1.952	0.013	0.730	0.009	-0.22	0.04
J122538+332654	186.4118	33.4486	21.223	0.009	20.71	0.16	1.696	0.016	0.657	0.013	-0.20	0.16
J122541+333109	186.4210	33.5194	21.903	0.016	20.28	0.05	2.709	0.035	1.058	0.020	0.52	0.06
J122544+333016	186.4354	33.5046	23.298	0.053	20.12	0.05	3.232	0.069	2.148	0.055	0.98	0.05
J122548+333802	186.4535	33.6341	21.255	0.010	20.70	0.08	1.939	0.016	0.738	0.013	-0.24	0.08
J122558+333154	186.4917	33.5318	23.479	0.062	20.88	0.10	2.977	0.079	1.877	0.066	0.67	0.10

(This table is available in machine-readable form.)

**Table 11**  
Colors of GCCs in NGC 4736

Name	R.A. J2000 deg	Decl. J2000 deg	$g'_0$ mag	$\Delta g'_0$ mag	$K_{s,0}$ mag	$\Delta K_{s,0}$ mag	$(u^* - i')_0$ mag	$\Delta (u^* - i')_0$ mag	$(g' - r')_0$ mag	$\Delta (g' - r')_0$ mag	$(g' - i')_0$ mag	$\Delta (g' - i')_0$ mag	$(i' - K_s)_0$ mag	$\Delta (i' - K_s)_0$ mag
J124947+411056	192.4496	41.1823	22.850	0.048	20.28	0.05	3.226	0.063	1.166	0.053	1.545	0.060	0.97	0.06
J124951+411538	192.4633	41.2606	19.098	0.008	18.57	0.01	1.717	0.010	0.425	0.010	0.667	0.012	-0.20	0.01
J125001+411350	192.5053	41.2307	20.147	0.014	19.71	0.02	1.699	0.017	0.419	0.018	0.661	0.022	-0.28	0.02
J125029+410951	192.6246	41.1644	21.591	0.027	20.95	0.05	1.743	0.032	0.492	0.033	0.737	0.041	-0.15	0.06
J125031+411039	192.6314	41.1777	22.573	0.053	21.28	0.07	2.711	0.076	0.612	0.063	0.850	0.076	0.39	0.09
J125031+410949	192.6329	41.1638	23.248	0.075	21.60	0.10	2.607	0.106	0.638	0.089	1.060	0.103	0.54	0.12
J125033+405708	192.6415	40.9525	19.946	0.012	19.49	0.01	1.821	0.014	0.399	0.015	0.647	0.019	-0.25	0.02
J125039+410913	192.6651	41.1538	22.044	0.039	21.40	0.09	1.884	0.048	0.482	0.048	0.690	0.060	-0.10	0.10
J125042+410345	192.6786	41.0625	23.082	0.061	19.81	0.02	3.000	0.040	1.320	0.067	2.358	0.068	0.86	0.04
J125043+410947	192.6807	41.1632	20.309	0.016	19.89	0.02	1.746	0.019	0.417	0.020	0.647	0.024	-0.28	0.03
J125045+410950	192.6902	41.1639	20.772	0.020	19.92	0.02	2.065	0.022	0.502	0.024	0.784	0.029	0.01	0.03
J125046+410210	192.6920	41.0361	19.819	0.014	18.47	0.01	2.688	0.014	0.587	0.016	0.923	0.019	0.37	0.01
J125051+410314	192.7138	41.0540	21.023	0.022	20.32	0.03	2.033	0.025	0.466	0.027	0.747	0.033	-0.10	0.04
J125051+411341	192.7148	41.2282	19.920	0.013	19.39	0.01	1.708	0.015	0.399	0.016	0.634	0.019	-0.16	0.02
J125056+410327	192.7340	41.0576	22.302	0.040	20.78	0.05	2.794	0.057	0.582	0.048	0.906	0.058	0.56	0.06
J125059+410949	192.7500	41.1637	21.343	0.026	20.56	0.04	2.130	0.030	0.516	0.031	0.745	0.038	-0.02	0.05
J125101+410046	192.7577	41.0128	22.393	0.042	21.26	0.08	2.136	0.050	0.560	0.050	0.844	0.060	0.23	0.09
J125104+410416	192.7698	41.0712	20.960	0.023	19.85	0.02	2.321	0.025	0.539	0.028	0.866	0.033	0.19	0.03
J125108+410404	192.7848	41.0679	22.459	0.043	21.60	0.11	1.984	0.053	0.523	0.052	0.755	0.063	0.05	0.12
J125110+410856	192.7957	41.1491	20.314	0.017	19.81	0.02	1.753	0.020	0.403	0.021	0.646	0.026	-0.20	0.03
J125120+410710	192.8362	41.1197	21.730	0.029	20.51	0.04	2.473	0.037	0.546	0.035	0.790	0.043	0.38	0.05
J125130+410551	192.8767	41.0977	21.431	0.025	20.92	0.06	1.714	0.030	0.434	0.031	0.657	0.039	-0.20	0.07
J125131+410849	192.8828	41.1472	19.149	0.009	18.68	0.01	1.743	0.010	0.399	0.011	0.633	0.013	-0.22	0.01
J125143+410606	192.9315	41.1018	20.757	0.018	20.10	0.04	2.027	0.021	0.469	0.022	0.678	0.027	-0.07	0.04
J125147+410439	192.9478	41.0776	21.403	0.026	20.16	0.04	2.570	0.030	0.548	0.031	0.871	0.037	0.32	0.05

(This table is available in machine-readable form.)

**Table 12**  
Colors of GCCs in NGC 4826

Name	R.A. J2000 deg	Decl. J2000 deg	$g'_0$ mag	$\Delta g'_0$ mag	$K_{s,0}$ mag	$\Delta K_{s,0}$ mag	$(u^* - i')_0$ mag	$\Delta (u^* - i')_0$ mag	$(g' - r')_0$ mag	$\Delta (g' - r')_0$ mag	$(g' - i')_0$ mag	$\Delta (g' - i')_0$ mag	$(i' - K_s)_0$ mag	$\Delta (i' - K_s)_0$ mag
J125549+213423	193.9550	21.5733	19.982	0.009	19.36	0.03	2.011	0.007	0.424	0.011	0.665	0.011	-0.17	0.03
J125601+214923	194.0083	21.8233	21.238	0.018	20.26	0.03	1.854	0.013	0.811	0.021	1.027	0.021	-0.17	0.03
J125612+214638	194.0522	21.7773	22.550	0.033	21.38	0.09	2.465	0.044	0.484	0.040	0.810	0.040	0.23	0.10
J125613+214412	194.0544	21.7368	22.804	0.034	19.36	0.01	3.273	0.027	1.946	0.036	2.331	0.036	0.98	0.02
J125614+214043	194.0592	21.6789	21.255	0.016	20.17	0.02	1.983	0.013	0.730	0.019	0.956	0.019	0.01	0.03
J125615+214645	194.0648	21.7794	20.949	0.015	20.30	0.03	1.958	0.013	0.349	0.019	0.625	0.019	-0.10	0.03
J125622+215134	194.0944	21.8597	21.335	0.017	20.39	0.05	2.067	0.014	0.716	0.020	0.952	0.020	-0.14	0.05
J125623+214054	194.0982	21.6817	21.091	0.015	19.85	0.02	1.841	0.011	0.972	0.017	1.096	0.018	0.02	0.02
J125625+214427	194.1082	21.7408	20.446	0.013	19.72	0.02	1.894	0.010	0.355	0.016	0.638	0.015	-0.04	0.02
J125626+213440	194.1095	21.5779	20.705	0.013	20.34	0.03	1.706	0.011	0.266	0.017	0.516	0.017	-0.27	0.03
J125626+214234	194.1124	21.7096	20.816	0.013	19.95	0.02	1.901	0.011	0.530	0.016	0.851	0.016	-0.11	0.02
J125628+214937	194.1207	21.8272	20.872	0.014	19.38	0.01	1.956	0.011	0.954	0.016	1.198	0.017	0.17	0.02
J125632+214023	194.1364	21.6733	21.338	0.018	20.55	0.04	1.850	0.016	0.335	0.023	0.624	0.023	0.04	0.04
J125633+213919	194.1416	21.6554	20.733	0.013	20.01	0.02	1.710	0.010	0.538	0.015	0.743	0.016	-0.15	0.03
J125638+214512	194.1583	21.7535	23.490	0.049	21.22	0.08	2.774	0.053	1.230	0.054	1.678	0.054	0.47	0.08
J125641+213802	194.1709	21.6341	21.815	0.021	20.74	0.05	1.862	0.016	0.762	0.025	1.020	0.025	-0.07	0.05
J125641+213641	194.1734	21.6115	20.810	0.013	19.93	0.02	2.026	0.011	0.494	0.016	0.760	0.016	-0.00	0.02
J125642+213204	194.1761	21.5347	21.075	0.016	20.35	0.03	1.940	0.014	0.352	0.020	0.612	0.020	-0.01	0.03
J125644+213848	194.1873	21.6468	20.897	0.014	19.90	0.02	1.755	0.010	0.808	0.016	0.979	0.016	-0.11	0.02
J125646+213754	194.1954	21.6317	21.352	0.018	20.72	0.04	1.768	0.016	0.314	0.023	0.562	0.023	-0.05	0.05
J125649+214425	194.2065	21.7404	21.212	0.016	20.01	0.02	2.093	0.012	0.787	0.019	0.993	0.019	0.09	0.02
J125654+215233	194.2275	21.8760	22.006	0.026	19.70	0.04	3.167	0.028	1.013	0.029	1.297	0.029	0.88	0.04
J125655+213319	194.2323	21.5554	21.993	0.023	21.18	0.06	1.729	0.020	0.707	0.028	0.960	0.028	-0.27	0.06
J125655+214633	194.2332	21.7761	20.895	0.015	20.32	0.03	1.830	0.013	0.391	0.018	0.587	0.018	-0.14	0.03
J125714+213914	194.3117	21.6540	19.931	0.009	19.66	0.02	1.805	0.008	0.271	0.012	0.466	0.012	-0.32	0.02
J125717+213702	194.3225	21.6173	21.816	0.022	20.73	0.04	1.887	0.016	0.789	0.025	0.990	0.026	-0.03	0.04
J125721+213816	194.3410	21.6378	22.215	0.028	19.73	0.02	3.257	0.032	0.998	0.031	1.343	0.031	1.01	0.02
J125722+213659	194.3418	21.6166	20.674	0.013	19.80	0.02	1.784	0.009	0.705	0.015	0.961	0.015	-0.21	0.02
J125723+214212	194.3472	21.7036	20.805	0.015	20.36	0.04	1.689	0.012	0.301	0.019	0.528	0.018	-0.21	0.04
J125723+213711	194.3480	21.6198	20.644	0.014	20.18	0.03	1.754	0.011	0.324	0.018	0.493	0.017	-0.16	0.03

(This table is available in machine-readable form.)

**Table 13**  
Parameters of Double Gaussian Fits to Color Distributions

Color	Parameter	NGC 3368	NGC 4395	NGC 4736	NGC 4826
$(u^* - g')_0$	$\mu_1$	1.23	1.12	1.07	1.08
	$\sigma_1$	0.07	0.06	0.03	0.21
	$N_1$	12	9	7	27
	$\mu_2$	1.53	1.651	1.40	1.83
	$\sigma_2$	0.05	0.001	0.31	0.10
	$N_2$	3	1	18	3
$(u^* - i')_0$	$\mu_1$	1.97	1.85	1.86	1.87
	$\sigma_1$	0.13	0.10	0.16	0.11
	$N_1$	11	7	16	25
	$\mu_2$	2.54	2.97	2.66	2.98
	$\sigma_2$	0.12	0.21	0.30	0.32
	$N_2$	4	3	9	5
$(g' - r')_0$	$\mu_1$	...	...	0.49	0.61
	$\sigma_1$	...	...	0.07	0.27
	$N_1$	...	...	23	29
	$\mu_2$	...	...	1.24	1.946
	$\sigma_2$	...	...	0.08	0.001
	$N_2$	...	...	2	1
$(g' - i')_0$	$\mu_1$	0.78	0.72	0.75	0.82
	$\sigma_1$	0.13	0.06	0.10	0.24
	$N_1$	14	7	23	28
	$\mu_2$	1.539	1.66	1.72	1.81
	$\sigma_2$	0.001	0.49	0.55	0.46
	$N_2$	1	3	2	2
$(g' - K_s)_0$	$\mu_1$	0.63	0.50	0.79	0.71
	$\sigma_1$	0.24	0.13	0.38	0.28
	$N_1$	12	7	23	26
	$\mu_2$	1.28	2.39	2.87	2.45
	$\sigma_2$	0.43	0.67	0.35	0.53
	$N_2$	3	3	2	4
$(r' - i')_0$	$\mu_1$	...	...	0.27	0.24
	$\sigma_1$	...	...	0.05	0.04
	$N_1$	...	...	24	24
	$\mu_2$	...	...	1.038	0.28
	$\sigma_2$	...	...	0.001	0.09
	$N_2$	...	...	1	6

solid red lines are Gaussians with the expected characteristics of the luminosity functions: mean = 22.0 mag,  $\sigma = 1.2$  mag for NGC 3368; mean = 20.1 mag,  $\sigma = 0.9$  mag for NGC 4395; mean = 20.4 mag,  $\sigma = 1.2$  mag for NGC 4736; mean = 21.2 mag, and  $\sigma = 1.1$  mag for NGC 4826. The curves have been scaled such that their integrals are equal to the expected GCCs for each galaxy, respectively, 35, 15, 46, and 69, for NGC 3368, NGC 4395, NGC 4736, and NGC 4826 (see Section 7 and Table 10).

We also take the opportunity here to stress that we do not use the extrapolation over the luminosity function to derive the total number of globular clusters in the system. We perform the completeness and GCLF corrections implicitly, as we explain in the next section.

## 7. Total Number of GCs

### 7.1. Correction for Incomplete Spatial Coverage

Given the small number of clusters detected, and the lack of constraints in the centermost regions of the galaxies due to confusion, here we derive the total number of GCs for each

galaxy through a comparison with the GC system of the MW. The procedure was introduced by Kissler-Patig et al. (1999), who applied it to edge-on spirals; its results are consistent with those from a fit to the radial number density, when both methods can be applied to the same object (Kissler-Patig et al. 1999; Goudfrooij et al. 2003). González-Lópezlira et al. (2017) adapted it for use on any galaxy, regardless of orientation. With this method, the correction for incomplete spatial coverage implicitly takes care of the completeness correction and the extrapolation over the luminosity function.

In brief, the method consists in estimating the number of GCs that one would detect if the MW were at the distance and orientation of the galaxy of interest, and were observed with the same instrument and to the same depth. By comparison, the total number of GCs would be

$$N_{\text{GC}} = N_{\text{GC}}(\text{MW}) \frac{N_{\text{obs}}}{N_{\text{FOV}}} \quad (3)$$

$N_{\text{GC}}(\text{MW})$  is the total number of clusters in the MW, including objects invisible to us behind the bulge;  $N_{\text{obs}}$  is the number of clusters observed in the target galaxy, and  $N_{\text{FOV}}$  is the number

**Table 14**  
Single Gaussian Fits to the Colors of the GC Systems of the MW and M31

System	$(u^* - g')$		$(u^* - g')_0$		$(u^* - i')$		$(u^* - i')_0$		$(g' - r')$		$(g' - r')_0$		$(g' - i')$		$(g' - i')_0$		$(g' - K_s)$		$(g' - K_s)_0$		$(r' - i')$		$(r' - i')_0$	
	$\mu$	$\sigma$	$\mu$	$\sigma$	$\mu$	$\sigma$	$\mu$	$\sigma$	$\mu$	$\sigma$	$\mu$	$\sigma$	$\mu$	$\sigma$	$\mu$	$\sigma$	$\mu$	$\sigma$	$\mu$	$\sigma$	$\mu$	$\sigma$	$\mu$	$\sigma$
M31	1.30	0.26	1.05	...	2.29	0.53	1.72	...	0.64	0.17	0.45	...	1.00	0.28	0.68	...	1.24	0.61	0.56	...	0.36	0.12	0.23	...
MW	...	...	1.01	0.15	...	...	1.67	0.26	...	...	0.45	0.09	...	...	0.66	0.12	...	...	...	...	...	...	0.21	0.03

**Note.** We remind the reader that colors using the new  $u^*$  filter are  $\sim 0.2$  mag redder. The colors of the M31 GCs were transformed by González-Lópezlira et al. (2017) to the previous CFHT system.

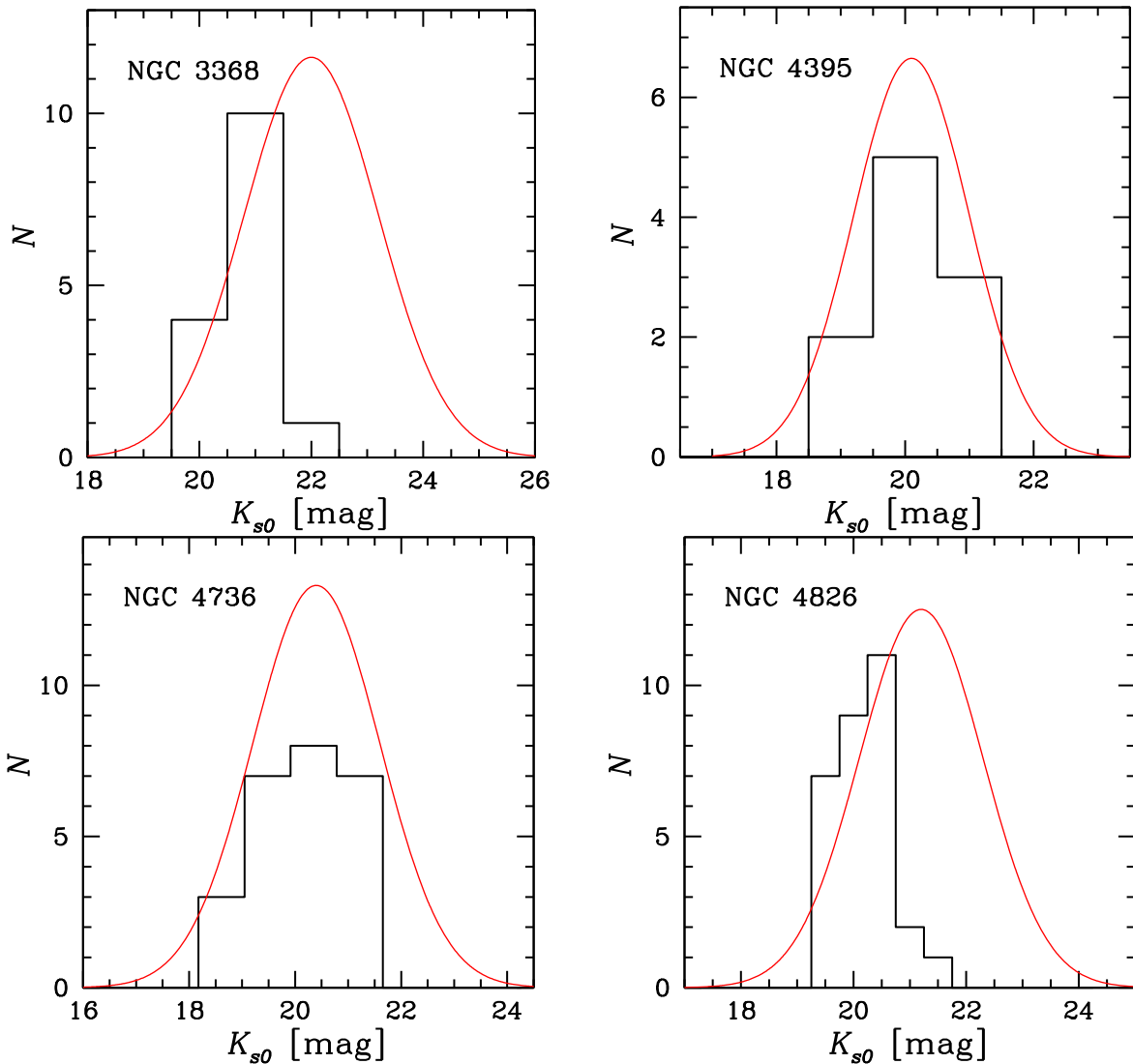


**Figure 12.**  $K_s$ -band luminosity functions of the GCCs. Top left: NGC 3368; top right: NGC 4395; bottom left: NGC 4736; bottom right: NGC 4826. Histograms: number of detected objects; solid red lines: expected Gaussian GCLFs (see Table 4 and Section 7).

of objects recovered in the artificial observation of the MW. We take  $N_{\text{GC}}(\text{MW}) = 160 \pm 10$  (Harris et al. 2014).

In order to estimate  $N_{\text{FOV}}$  we use the catalog by Harris (1996), which provides  $X$ ,  $Y$ ,  $Z$  coordinates for 144 MW GCs. The origin of this coordinate system is at the position of the Sun; the  $X$ -axis points toward the Galactic Center, the  $Y$  axis points in the direction of Galactic rotation, and  $Z$  is perpendicular to the Galactic plane. We define a new coordinate system,  $X'YZ$ , with origin in the Galactic Center, assuming a Galactocentric distance for the Sun  $R_0 = 8.34$  kpc (Reid et al. 2014). For galaxies that are not edge-on, we first rotate the MW GC system in 3D by the inclination angle  $i$  of the target galaxy (i.e.,  $46.2^\circ$  for NGC 3368,  $33.7^\circ$  for NGC 4395,  $35.6^\circ$  for NGC 4736 and  $57.5^\circ$  for NGC 4826) with respect to either the  $X'$  or  $Y$ -axis, then project it on the plane of the sky; the rotated pairs  $(X'_{\text{rot},X'}, Y_{\text{rot},X'})$ ,  $(X'_{\text{rot},Y}, Y_{\text{rot},Y})$ , where the subscript indicates the Galactic axis of 3D rotation, are directly the projected coordinates. The easiest way to place the projected system on the WIRCam FOV is to then apply a rotation around the line of sight equal to the PA of the target galaxy ( $5^\circ$  for NGC 3368,  $147^\circ$  for NGC 4395, and  $115^\circ$  for both NGC 4736 and NGC 4826, always north through east).

To ensure a fair comparison with the MW, we then mask out elliptical regions in the centers of the galaxies. For NGC 4395, NGC 4736, and NGC 4826, they have the same axis ratios [i.e.,  $\cos(i)$ ] and PA as the galaxies. Their semimajor axes are equal to, respectively,  $98.9''$ ,  $168.3''$ , and  $150''$ , or  $0.25 R_{25}$  for NGC 4395, and  $0.5 R_{25}$  for both NGC 4736 and NGC 4826. For NGC 3368, we exclude an ellipse with an axis ratio  $0.69$  and PA  $= 155^\circ$ , like the region in the galaxy with the highest surface brightness, and semimajor axis equal to  $85.6''$ , or  $0.375 R_{25}$  (de Vaucouleurs et al. 1991). These are the areas most affected by confusion (see Section 4 and Figures 2 and 3). We also need to set detection limits for these simulated observations. To this end, we combine the real limiting magnitude of the  $K_s$  images, with the difference between the  $K_s$  and  $V$  bands TO magnitudes; the results are  $V = 22.5$ ,  $21.6$ ,  $23.4$ , and  $23.1$  mag, respectively, for NGC 3368, NGC 4395, NGC 4736, and NGC 4826. Finally, the  $V$  mag of each MW cluster is corrected for the Galactic extinction given in the Harris (1996) catalog, and subsequently dimmed by the foreground extinction in the direction of each galaxy, i.e.,  $0.069$  mag (NGC 3368),  $0.047$  mag (NGC 4395),  $0.049$  mag (NGC 4736), and  $0.113$  mag (NGC 4826), respectively.

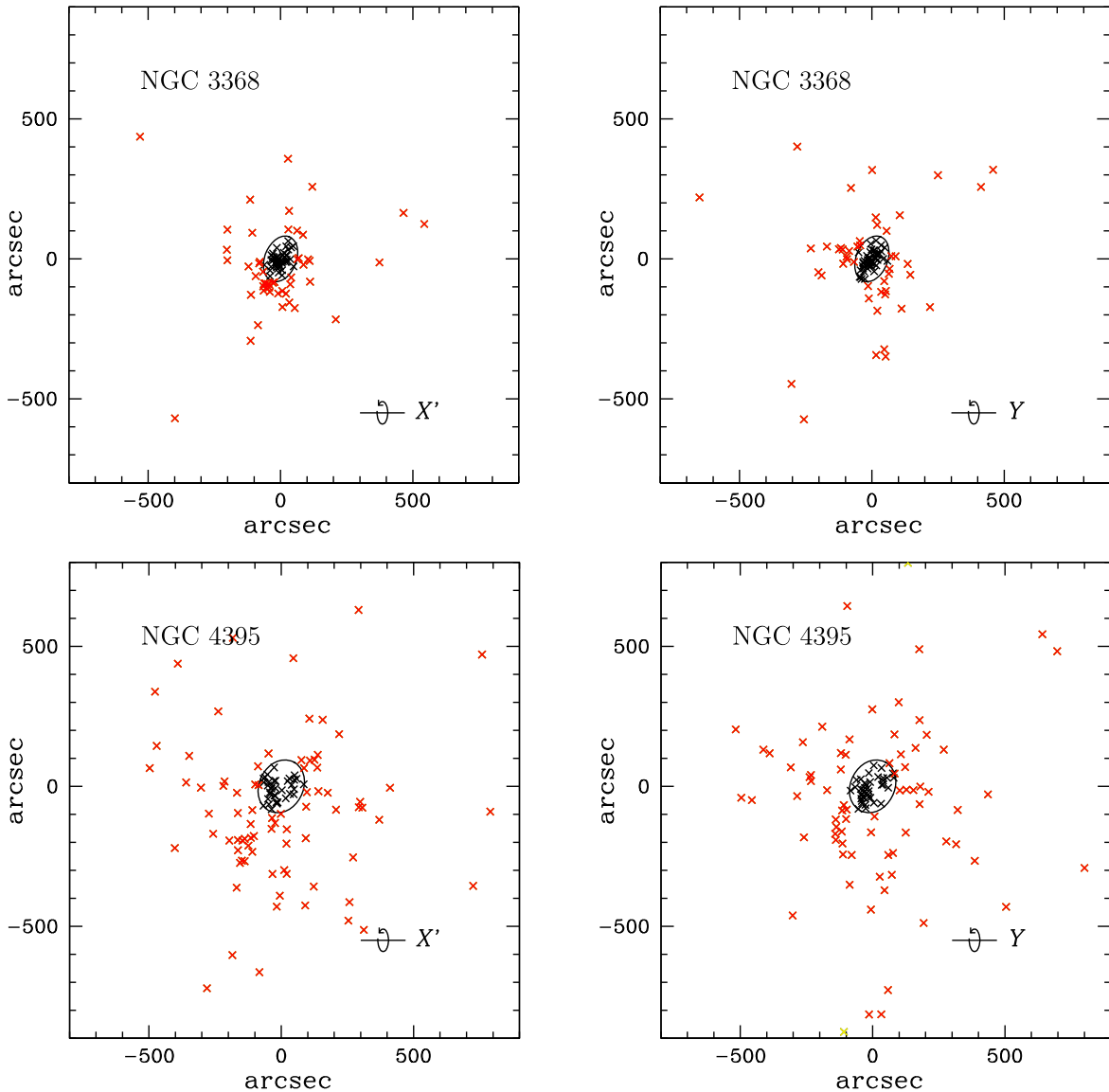


**Figure 13.** MW GC system, at the distance and orientation of studied galaxies, projected coordinates  $+X_{\text{proj}}$ ,  $+Y_{\text{proj}}$ . Top: NGC 3368; bottom: NGC 4395. Left: 3D rotation about the Galactic  $X'$ -axis before projection on the plane of the sky. Right: 3D rotation about Galactic  $Y$ -axis. Solid black line: mask; red crosses: sources visible in the WIRCam FOV; yellow crosses: recovered in the simulation, but outside of the WIRCam FOV; black crosses: masked-out GCs.

For every galaxy, there are four possible orientations of the FOV and mask that preserve its alignment; they can be seen as mirror reflections of the projected coordinates ( $+X_{\text{proj}}$ ,  $+Y_{\text{proj}}$ ;  $+X_{\text{proj}}$ ,  $-Y_{\text{proj}}$ ;  $-X_{\text{proj}}$ ,  $+Y_{\text{proj}}$ ;  $-X_{\text{proj}}$ ,  $-Y_{\text{proj}}$ ), with two sets of four pairs, i.e., one for each of the two possible rotation axes).

We show in Figures 13 and 14 the results of the artificial observations of the MW GC system, for the rotation around the  $X'$  (left) and  $Y$  (right) axes, respectively, and  $+X_{\text{proj}}$ ,  $+Y_{\text{proj}}$ . Results for NGC 3368 and NGC 4395 are displayed, respectively, in the top and bottom panels of Figure 13, whereas outcomes for NGC 4736 and NGC 4826 are presented in the top and bottom panels of Figure 14. Angular distances in arcsec are measured relative to the centers of the galaxies, with the horizontal axis increasing in the direction of decreasing R.A. The ellipses delineated with the black solid line mark the outer edges of the masks; the red crosses are clusters visible in the WIRCam FOV, while sources that have been masked out are represented by black crosses.

In the case of NGC 3368, for the four realizations rotating around the  $X'$ -axis we detect, respectively, 50 ( $+X_{\text{proj}}$ ,  $+Y_{\text{proj}}$ ), 50 ( $+X_{\text{proj}}$ ,  $-Y_{\text{proj}}$ ), 50 ( $-X_{\text{proj}}$ ,  $+Y_{\text{proj}}$ ), and 50 ( $-X_{\text{proj}}$ ,  $-Y_{\text{proj}}$ ) sources; for rotating around the  $Y$ -axis, the numbers are 46, 46, 46, and 46. With these numbers, there would be, on average,  $48 \pm 2$  simulated clusters visible in NGC 3368, and Equation (3) gives a total  $N_{\text{GC}} = 50 \pm 13$ . This error is statistical only; it includes errors in the assumed number of total GCs in the MW, Poisson errors in the observed number of GCCs in NGC 3368, and Poisson errors in the number of simulated clusters in the WIRCam FOV. To this error, we add potential systematics. Errors in the distance to NGC 3368 result in uncertainties in the detection limiting magnitude, and in the effective areas of the galaxy covered by the FOV and excluded by the mask. For the given uncertainty in the distance to NGC 3368 ( $^{+1.1}_{-1.0}$  Mpc),  $N_{\text{GC}}$  would vary by  $+21/-14$  if the random and systematic errors are added in quadrature. Another potential concern is that the MW and NGC 3368 likely have a different number of obscured clusters. To account for this

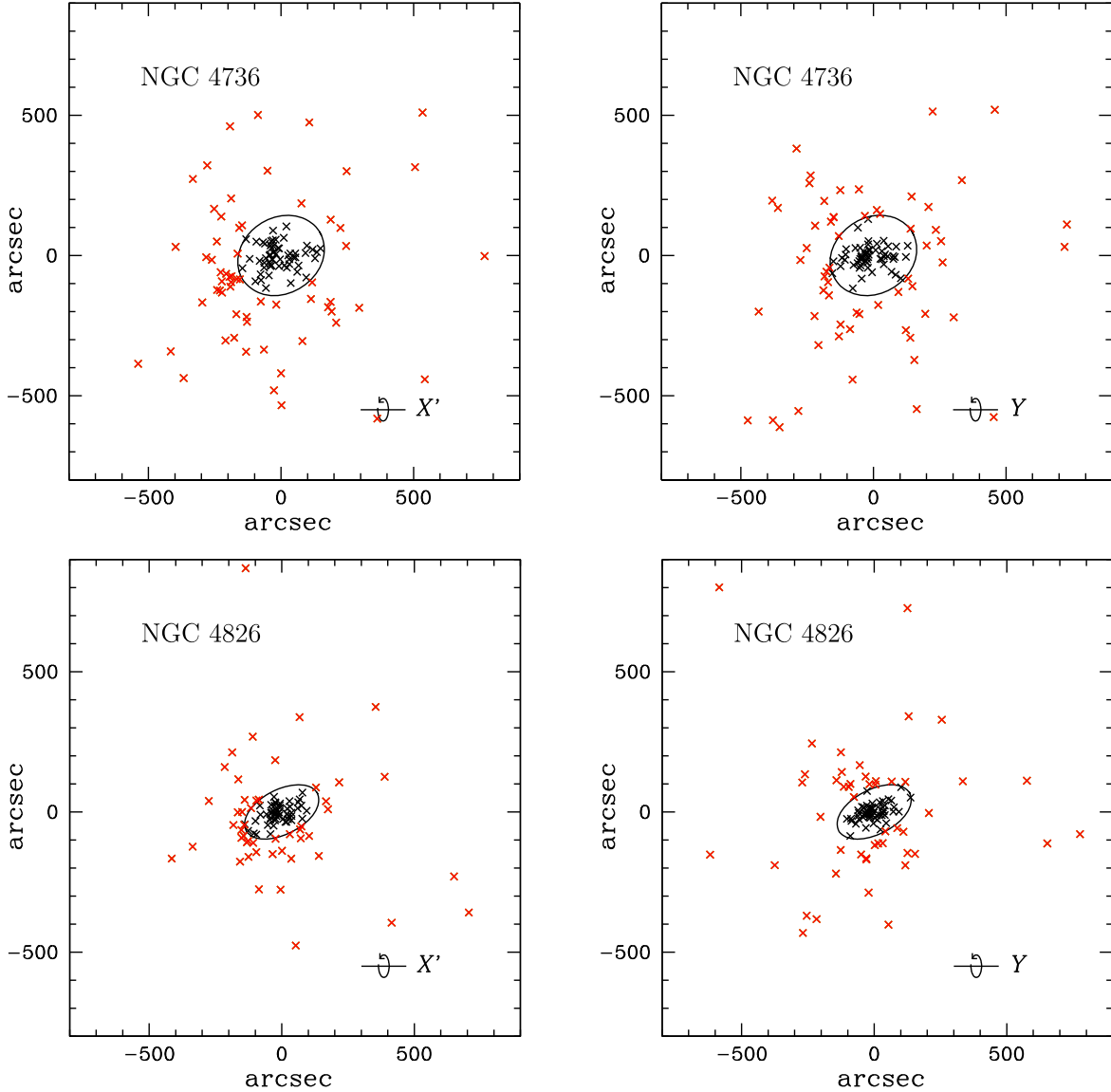


**Figure 14.** MW GC system, at the distance and orientation of studied galaxies, projected coordinates  $+X_{\text{proj}}$ ,  $+Y_{\text{proj}}$ . Top: NGC 4736; bottom: NGC 4826. Symbols as in Figure 13.

possibility, we include an additional uncertainty of 25% ( $\pm 12$ ). We end up with  $N_{\text{GC}} = 50^{+24}_{-19}$ , or  $50 \pm 13^{+20}_{-13}$ , with the first error statistical and the second, systematic (from distance and differential obscuration).

For NGC 4395, rotations around  $X'$  yield 80, 80, 80, 79; for the  $Y$ -axis, the results are 73, 71, 75, 71. Therefore, the average simulated clusters visible would be  $76 \pm 4$ , and a total  $N_{\text{GC}} = 21 \pm 5$  from Equation (3). The distance uncertainty of  $\pm 0.4$  Mpc results in an additional error of  $\pm 1$  in  $N_{\text{GC}}$ . Including a 25% ( $\pm 6$ ) uncertainty for differential obscuration, the census for NGC 4395 is  $N_{\text{GC}} = 21 \pm 8$ , or  $21 \pm 5 \pm 6$ .

For NGC 4736, we find, respectively, 62, 62, 62, and 61 for rotations around  $X'$ ; for the  $Y$ -axis, the results are 60, 60, 61, and 60. Hence, the average simulated clusters visible would be  $61 \pm 1$ , and a total  $N_{\text{GC}} = 66 \pm 14$  from Equation (3). The distance uncertainty of  $\pm 0.4$  Mpc results in an additional error of  $+6/-3$  in  $N_{\text{GC}}$ . Including a 25% ( $\pm 16$ ) uncertainty for differential obscuration, the tally for NGC 4736 is  $N_{\text{GC}} = 66^{+22}_{-21}$ , or  $66 \pm 14^{+17}_{-16}$ .

Finally, for NGC 4826, rotations around  $X'$  give 49, 49, 50, and 49 detections; for the  $Y$ -axis, the results are 48, 47, 47, and 48. Accordingly, the average simulated clusters visible would be  $48 \pm 1$ , and a total  $N_{\text{GC}} = 99 \pm 19$  from Equation (3). The distance uncertainty of  $\pm 0.7$  Mpc results in an additional error of  $+20/-10$  in  $N_{\text{GC}}$ . Including a 25% ( $\pm 25$ ) uncertainty for differential obscuration, the count for NGC 4826 is  $N_{\text{GC}} = 99^{+37}_{-33}$ , or  $99 \pm 19^{+32}_{-21}$ .

We make a final, downward, correction of 30% to these numbers, based on the percentage contamination found for NGC 4258 by González-Lópezlira et al. (2019), from spectroscopic observations of its GC candidates. Hence, we get  $N_{\text{GC}} = 35^{+20}_{-16}$  for NGC 3368,  $N_{\text{GC}} = 15 \pm 7$  for NGC 4395,  $N_{\text{GC}} = 46 \pm 18$  for NGC 4736, and  $N_{\text{GC}} = 69^{+31}_{-28}$  for NGC 4826.

The correlation of  $N_{\text{GC}}$  with virial mass provides an additional sanity check, at least for NGC 4736 and NGC 4826. From their rotation curves (respectively, Jatlocha et al. 2008 and Saburova et al. 2009), both galaxies are quite light, with total halo masses  $\sim 4 \times 10^{10} M_{\odot}$ ; their  $\log N_{\text{GC}} \sim 1.7$

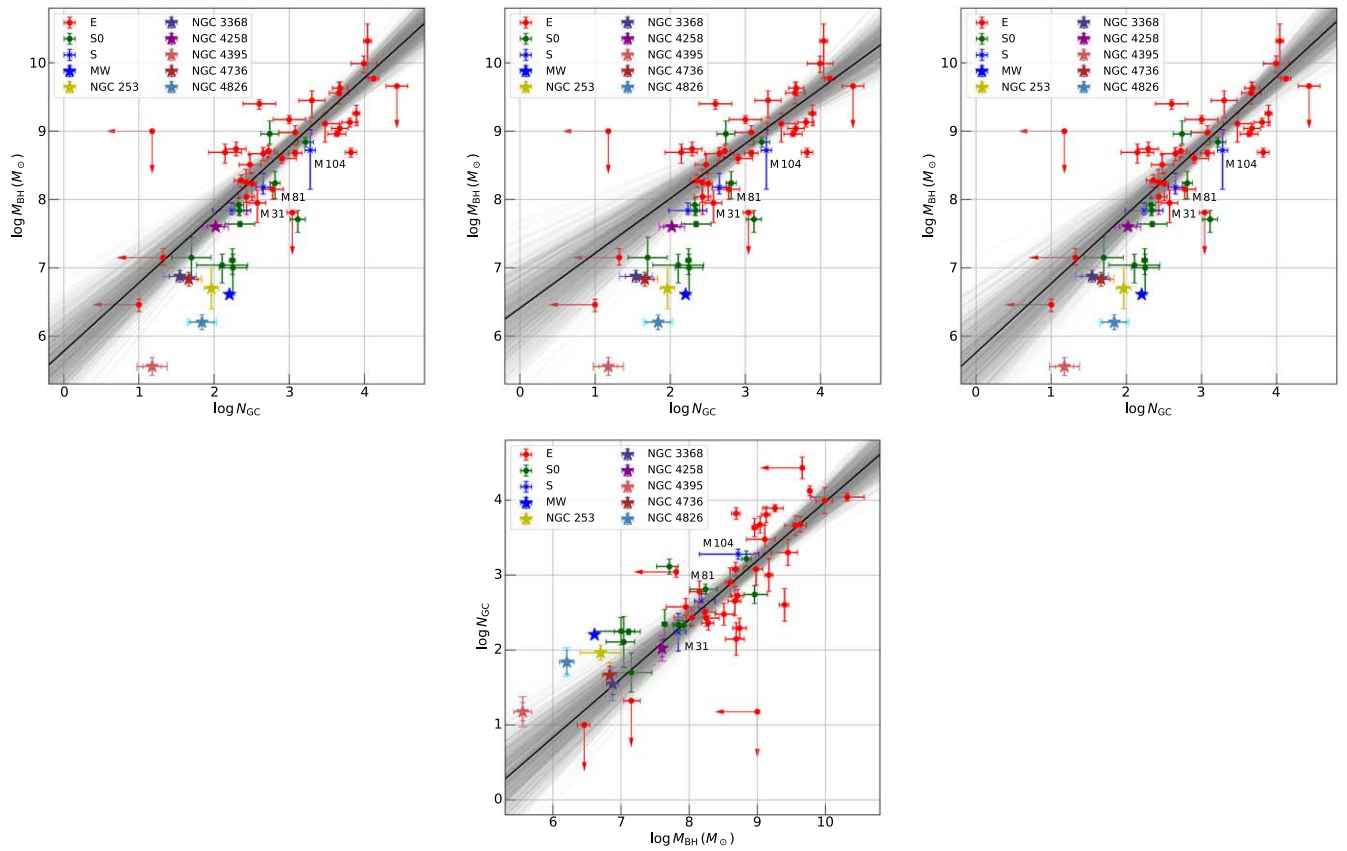


**Figure 15.** BCES fits to elliptical galaxies. *Top:*  $\log M_*$  vs.  $\log N_{\text{GC}}$ ; *bottom:*  $\log N_{\text{GC}}$  vs.  $\log M_*$ . *Left:* no additional scatter; *center:* additional  $\epsilon_y$ ; *right:*  $\epsilon_y$  and  $\epsilon_x$ . *Solid black lines:* best fits; *translucent gray lines:* range of possible solutions. Solid (red) and open (green) circles represent, respectively, elliptical and lenticular galaxies in the sample of Harris et al. (2014), reclassified as per Sahu et al. (2019b); the blue crosses are the spiral galaxies M 31, M 81, and M 104. *Solid blue star:* Milky Way. *Solid light olive star:* NGC 253, with correct number of GCs. *Solid purple star:* NGC 4258 (González-Lópezlira et al. 2017, 2019); *Solid violet, light brown, dark brown, and light blue stars:* NGC 3368, NGC 4395, NGC 4736, and NGC 4826, respectively (this work). For NGC 3368, NGC 4395, NGC 4258, NGC 4736, and NGC 4826, random errors of  $N_{\text{GC}}$  are shown by small bars, while systematic errors, added in quadrature, are illustrated by the large bars. Errors for the MW are smaller than the blue star.

is fully consistent with the larger dispersion of the correlation at low masses (see Burkert & Forbes 2020, their Figure 1).<sup>14</sup>

## 8. Specific Frequency, and the $N_{\text{GC}}$ versus $M_*$ Relation

From the distance to NGC 3368 and the values of  $B_{\text{T},0} = 9.80 \pm 15$  mag and  $(B - V)_{\text{T},0} = 0.79 \pm 0.01$  given in de Vaucouleurs et al. (1991), we find  $M_V = -21.08 \pm 0.36$  mag, and a specific frequency  $S_N = N_{\text{GC}} \times 10^{0.4 \times [M_V + 15]} = 0.13 \pm 0.06$ , if we consider random errors only, and  $S_N = 0.13 \pm 0.07$ , if we include the uncertainty in the number of obscured clusters.<sup>15</sup> For NGC 4395, de Vaucouleurs et al. (1991) report  $B_{\text{T},0} = 10.57 \pm 0.54$  mag and  $(B - V)_{\text{T},0} = 0.46 \pm 0.08$  mag; this results in  $M_V = -18.06 \pm 0.59$  mag and  $S_N = 0.90 \pm 0.55$ , with statistical errors only, and  $S_N = 0.90 \pm 0.65$  if the uncertainty in the number of obscured clusters is included. For NGC 4736, the values are  $B_{\text{T},0} = 8.75 \pm 0.13$  mag and  $(B - V)_{\text{T},0} = 0.72 \pm 0.01$  mag, from which  $M_V = -20.46 \pm 0.21$  mag, and  $S_N = 0.30 \pm 0.10$ , with random errors only, and  $S_N = 0.30 \pm 0.13$ , if we include systematics. For NGC 4826, de

Vaucouleurs et al. (1991) give  $B_{\text{T},0} = 8.82 \pm 0.24$  mag and  $(B - V)_{\text{T},0} = 0.71 \pm 0.01$  mag;  $M_V = -21.21 \pm 0.32$  mag, and  $S_N = 0.23 \pm 0.09$  or  $S_N = 0.23 \pm 0.11$ , respectively, without and with the uncertainty in the number of obscured clusters. For comparison, the Milky Way has  $S_N = 0.5 \pm 0.1$  (Ashman & Zepf 1998).

Before placing our four galaxies on the  $N_{\text{GC}} - M_*$  correlation, we redetermine it in the Appendix for the sample in Harris et al. (2014), plus NGC 4258 and the spirals in this paper, albeit with updated galaxy classifications from Sahu et al. (2019b).

Figures 15 and 16, and Table 17 display the Bivariate Correlated Errors and Intrinsic Scatter (BCES, Akitas & Bershadsky 1996) fits for, respectively, ellipticals and spirals. The black solid lines represent the best fits, and the translucent gray lines illustrate the range of possible solutions. Each gray line corresponds to a realization of the fit, obtained by adding a random variable to each the slope  $\beta$  and the intercept  $\alpha$  of the best fit, drawn from the normal distributions of errors,  $\sigma_\beta$  and  $\sigma_\alpha$ . Since 1,000 realizations were obtained for each fit, roughly 50 gray lines (5% of the total 1,000) belong to fits separated by  $2\sigma$  or more from the best values. In the figures, ellipticals appear as solid red circles and lenticulars as solid dark green ones; the spirals M 31, M 81, and M 104 are the blue crosses. The locations of the MW, NGC 253, NGC 3378, NGC 4258, NGC 4395, NGC 4736, and NGC 4826 are shown as solid stars, respectively, blue, light olive, violet, purple, light brown, dark brown, and light blue. We correct the position of NGC 253, whose number of GC had been read

<sup>14</sup> We note here that, from their analysis of the NGC 4736 rotation curve, Jaločić et al. (2008) conclude that it violates the sphericity condition at large radii (i.e., mass ceases to increase with distance). Hence, the galaxy would not have a massive spherical halo and its mass distribution would be best fit with a disk model.

<sup>15</sup> The systematic error in the distance basically cancels out, because the absolute magnitude of the galaxy also changes.

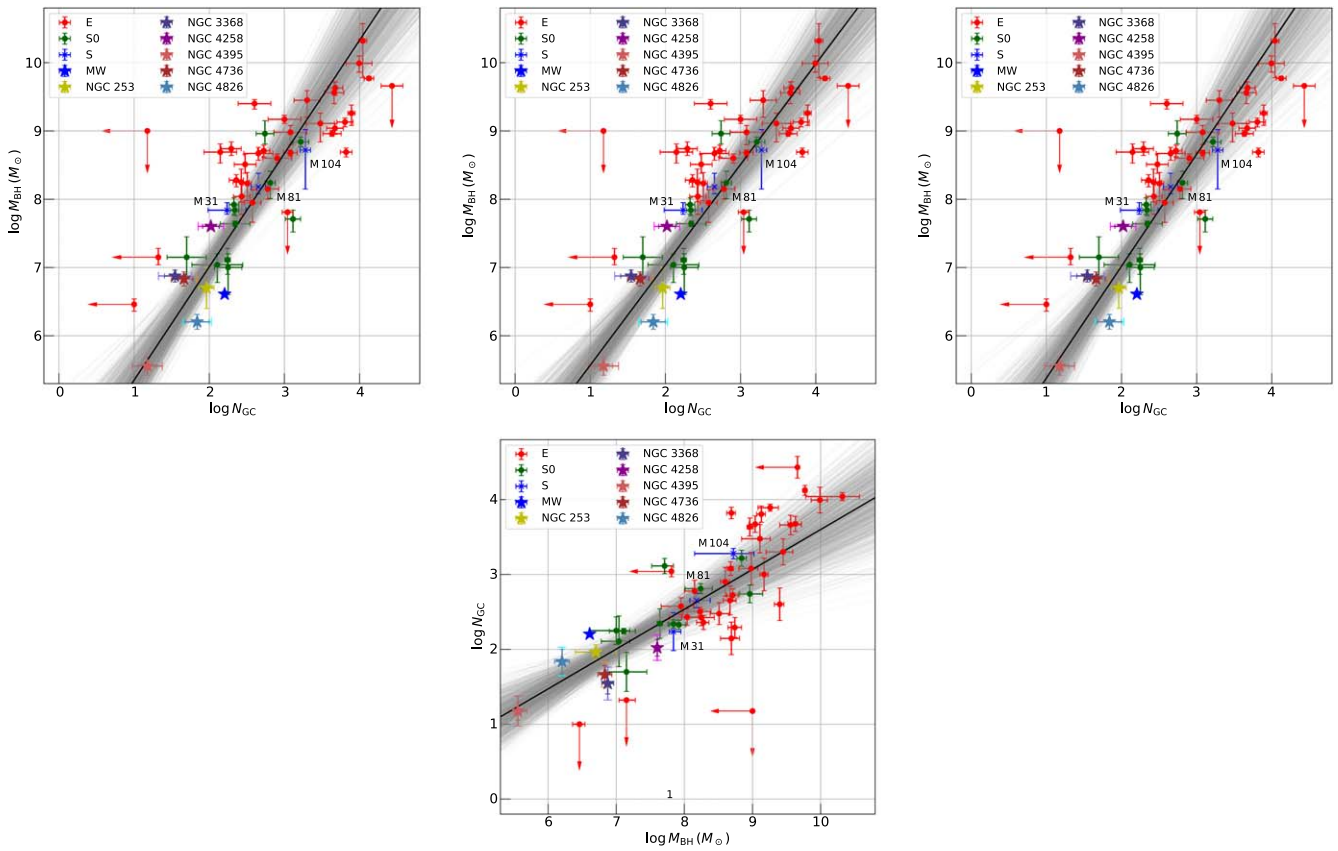


**Figure 16.** BCES fits to spiral galaxies. *Top:*  $\log M_*$  vs.  $\log N_{\text{GC}}$ ; *bottom:*  $\log N_{\text{GC}}$  vs.  $\log M_*$ . *Left:* no additional scatter; *center:* additional  $\epsilon_y$ ; *right:*  $\epsilon_y$  and  $\epsilon_x$ . Lines and symbols as in Figure 15.

erroneously by Harris et al. (2014). Indeed, Olsen et al. (2004) report  $N_{\text{GC}} = 21$ , but with a completeness of 0.21, i.e., they really implied  $N_{\text{GC}} \sim 100$ . They also give a specific frequency in the  $K$ -band  $S_{N,K} = N_{\text{GC}} \times 10^{0.4 \times [M_K + 18]} = 0.30 \pm 0.07$ , or  $N_{\text{GC}} = 92 \pm 21$ . Previously, Blecha (1986) had found  $N_{\text{GC}} = 80 \pm 40$  for NGC 253.

The Figures show  $M_*$  versus  $N_{\text{GC}}$  in the top row; from left to right, fits without extra “cosmic” scatter, fits with additional  $\epsilon_y$ , and fits with additional intrinsic scatter in both  $x$  and  $y$  (see Appendix). The bottom row illustrates  $N_{\text{GC}}$  versus  $M_*$ , only for fits with additional  $\epsilon_y$ , which are not symmetrical. We find that the slope of the correlation is roughly 60% steeper for spirals than for ellipticals (see Table 17).

## 9. The $M_*$ versus $M_*$ Correlation from NGC

In order to investigate whether the discrepant slopes of the  $M_*$  versus  $N_{\text{GC}}$  correlations for elliptical and spiral galaxies reflect the slopes between  $M_*$  and  $M_*$ , we derive  $M_*$  from its correlation with  $N_{\text{GC}}$ , for the ellipticals and LTGs in our sample. Hudson et al. (2014) have obtained  $\log M_{\text{GC}}$  versus  $\log M_*$  for the 422 galaxies (248 ellipticals, 93 lenticulars, and 81 spirals and irregulars) in the Harris et al. (2013) sample, where  $M_{\text{GC}}$  is the total mass of the GC system of a galaxy. In actuality,  $N_{\text{GC}}$  is the observable, while  $M_{\text{GC}}$  has the advantage of a smaller sensitivity to undetected faint GCs, since 99% of the total GC system mass is roughly contained in the clusters brighter than 1 mag below the GCLF turnover (González-Lópezlira et al. 2017).<sup>16</sup> Hudson et al. (2014) assume

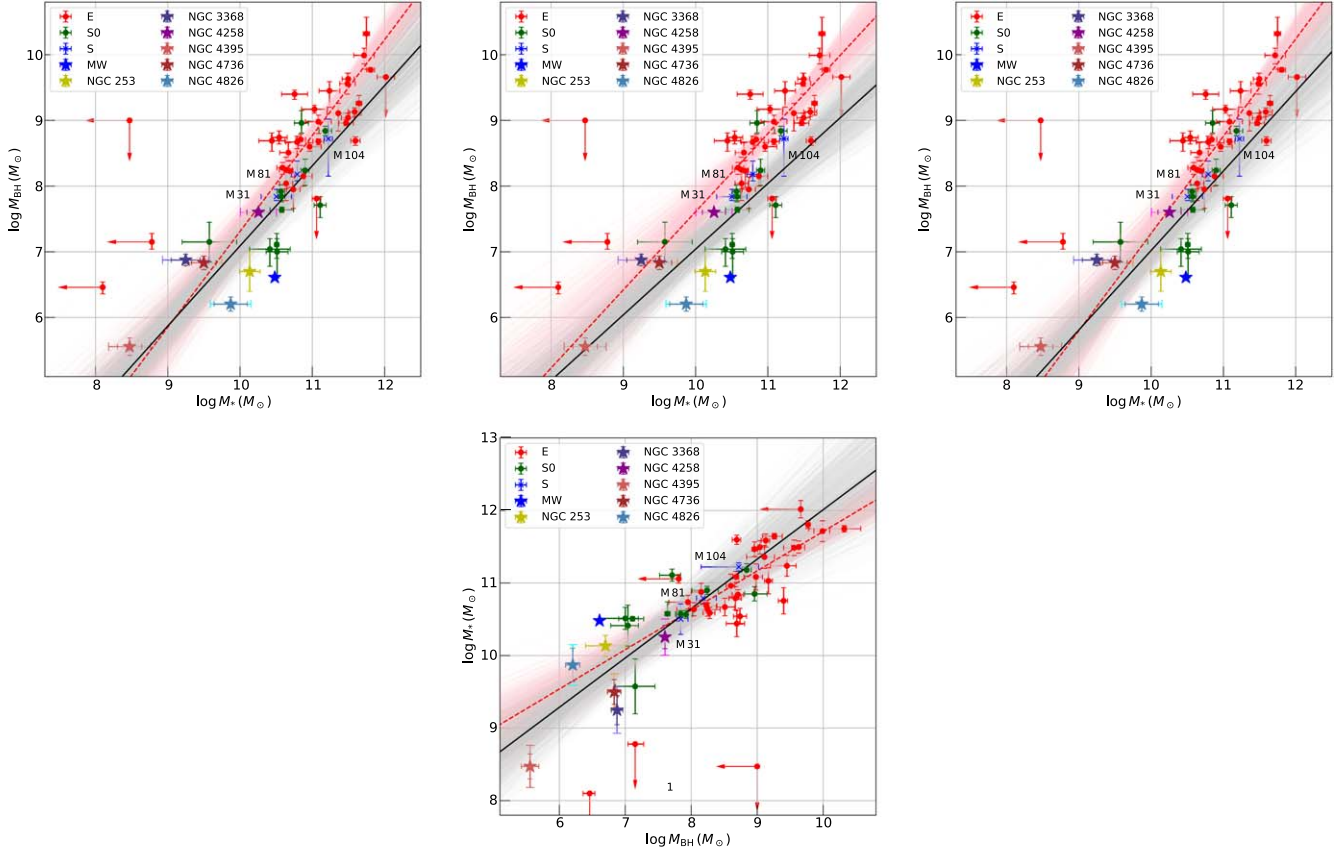
a relation between total number and total mass of GC  $\log N_{\text{GC}} = 0.90 \times M_{\text{GC}} - 4.65$ . The relations between  $\log M_{\text{GC}}$  or  $N_{\text{GC}}$  and  $M_*$  are broken power laws, with  $\log M_{\text{GC}} = 0.53 \times \log M_* + 2.00$ ,  $\log M_* = 2.11 \times \log N_{\text{GC}} + 5.99$ , for lower galaxy masses, and  $M_{\text{GC}} = 1.60 \times \log M_* - 9.22$ ,  $\log M_* = 0.69 \times \log N_{\text{GC}} + 8.96$ , for higher galaxy masses, with the inflection point at  $\log M_*/M_{\odot} \sim 10.4$ ,  $\log N_{\text{GC}} \sim 2.1$ .

Figure 17 and Table 19 show the BCES fits to  $M_*$  versus  $M_*$  for, respectively, ellipticals (red-dashed and pink translucent lines) and spirals (black solid and gray translucent lines). Their slopes are, roughly,  $1.47 \pm 0.16$  and  $1.22 \pm 0.15$ , respectively, i.e., the same within the errors, with the best fits as close or closer than those found by Reines & Volonteri (2015), also less steep for spirals than for ellipticals, and with an offset of  $\sim 0.2$ – $0.3$  dex at  $\log M_*/M_{\odot} = 10$ . A fit to both ellipticals and spirals together (Figure 18, Table 19) yields a slope of  $\sim 1.5 \pm 0.15$ , and a cosmic scatter  $\epsilon \sim 0.4$ , of the order of half that found by van den Bosch (2016).

## 10. Discussion and Conclusions

We have now successfully applied the  $u^*i'K_s$  diagram GC selection technique (Muñoz et al. 2014) to five spiral galaxies: NGC 4258 (González-Lópezlira et al. 2017), NGC 3368, NGC 4395, NGC 4736, and NGC 4826 (this work). We complement the  $u^*i'K_s$  plot with GCC structural parameters; this combination of techniques constitutes a very efficient tool to study GC systems of nearby galaxies. The sample of spirals with measurements of both the GC system and the SMBH mass has now been increased to 10, or 100% more than before we embarked on this project. Our full spiral working sample

<sup>16</sup> The trends of  $N_{\text{GC}}$  with total  $K$ -band luminosity, a good tracer of mass, are remarkably similar for all galaxy types.



**Figure 17.** BCES fits to elliptical and spiral galaxies. Top:  $\log M_*$  vs.  $\log M_{\bullet}$ ; bottom:  $\log M_*$  vs.  $\log M_{\bullet}$ . Left: no additional scatter; center: additional  $\epsilon_y$ ; right:  $\epsilon_y$  and  $\epsilon_x$ . Dashed red lines: best fits for ellipticals; translucent pink lines: range of possible solutions for ellipticals. Solid black lines: best fits for spirals; translucent gray lines: range of possible solutions for spirals. Symbols as in Figure 15.

comprises all galaxies observable from the northern hemisphere with a direct measurement of their central SMBH mass, and within 16 Mpc, regardless of orientation in the sky, i.e., a total of nine; so far, we have analyzed the five for which we have complete  $u^*$ ,  $i'$ , and  $K_s$  data. We have also taken the opportunity to correct the position of NGC 253 in the  $M_*$  versus the  $N_{\text{GC}}$  diagram.

The spiral galaxies for which we have determined  $N_{\text{GC}}$ , as well as NGC 253, seem to have undergone few major mergers. Like the MW, they all belong to small groups, i.e., Leo I, Canes I, Canes II, and Sculptor. They also have pseudobulges, except for NGC 4395, which is a bulgeless, purely disk galaxy. Additionally, the GC systems of both NGC 4258 and NGC 253 seem to lie in rotating disks (González-Lópezlira et al. 2019; Olsen et al. 2004). Together with simulations (e.g., Kravtsov & Gnedin 2005; Agertz et al. 2009; Kruijssen 2015) and observations of clumpy star-forming disks at  $z \sim 2$  (e.g., Cowie et al. 1995; Guo et al. 2015), the discovery of GC disks in the local universe supports the idea that GCs probably formed in disks, and came to populate halos through multiple mergers (e.g., Schweizer 1987; Ashman & Zepf 1992; Côté et al. 1998).

We have investigated the correlation between  $M_*$  and  $N_{\text{GC}}$ , for both ellipticals and LTG. We find  $\log M_* \propto (1.01 \pm 0.13) \log N_{\text{GC}}$  for ellipticals, and  $\log M_* \propto (1.64 \pm 0.24) \log N_{\text{GC}}$  for LTG, in both cases including cosmic scatter in both variables. Hence, they are not consistent with each other, and the slope of the correlation for LTG, in contrast with that for ellipticals, is not linear. This, together with the likely scarcity of major interactions for LTG, may argue in favor of statistical

convergence through mergers as the cause of the correlation in elliptical galaxies.

On the other hand, we have derived  $M_*$ , for the ellipticals and LTG in our sample, from its relation with  $N_{\text{GC}}$ , and measured the correlations with  $M_*$ . Far from mirroring the discrepant slopes of the  $M_*$  versus  $N_{\text{GC}}$  fits, they are quite similar, i.e.,  $M_* \propto (1.48 \pm 0.18) \log M_{\bullet}$  for ellipticals, and  $M_* \propto (1.21 \pm 0.16) \log M_{\bullet}$  for LTG, with a small offset of  $\sim 0.2\text{--}0.3$  dex at  $\log M_*/M_{\bullet} = 10$ , in both cases including cosmic scatter in both variables. These results are in line with those obtained by Reines & Volonteri (2015) and Simmons et al. (2017), and argue for a mostly nonmerger driven  $M_*$  growth, and galaxy black hole coevolution through secular processes, like calm accretion and feedback. (Simmons et al. 2017; Martin et al. 2018; Smethurst et al. 2019).

Researching GC systems and scaling relations in spirals is very important. While these relations in ellipticals seem to be showing the end result of star formation and galaxy assembly, in lower mass galaxies we may be witnessing the fingerprints of the individual steps of the process.

R.A.G.L. acknowledges the financial support of DGAPA, UNAM, project IN108518. R.A.G.L. and L.L.N. acknowledge the support of CONACYT, Mexico, project A1-S-8263. L.L. acknowledges the support of DGAPA PAPIIT grants IN112417 and IN112820, CONACYT-AEM grant 275201, and CONACYT-CF grant 263356. Y.O.-B. acknowledges support from FONDECYT Postdoctoral Fellowship project No. 3210442. We would like to thank the anonymous referee,

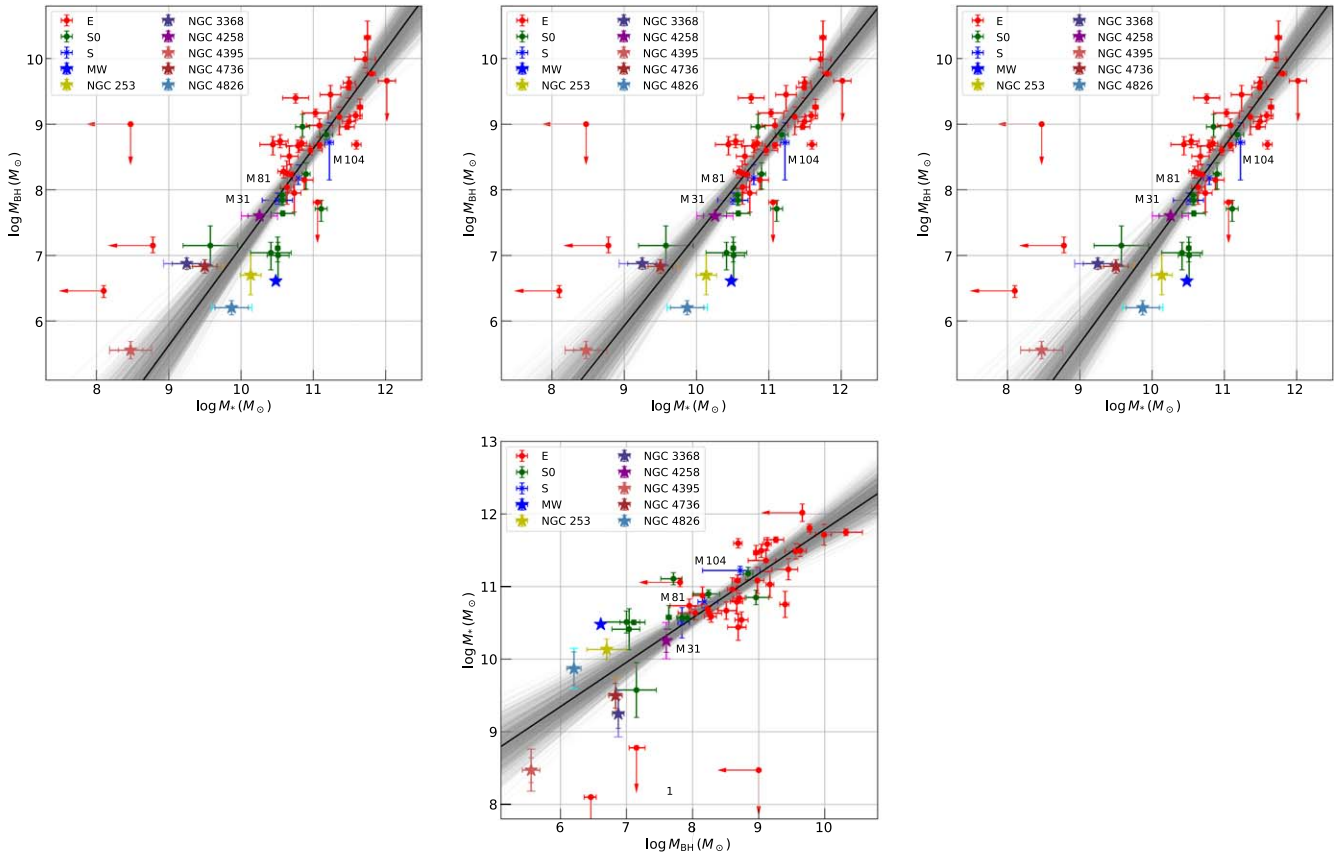


**Figure 18.** BCES fits to E+S galaxies. Top:  $\log M_*$  vs.  $\log M_{\bullet}$ ; bottom:  $\log M_{\bullet}$  vs.  $\log M_*$ . Left: no additional scatter; center: additional  $\epsilon_y$ ; right:  $\epsilon_y$  and  $\epsilon_x$ . Lines and symbols as in Figure 15.

for their pertinent criticisms and suggestions, and Daniel Díaz-González, for his help with the routine we used to calculate two-Gaussian fits.

This research has made use of the VizieR catalog access tool, CDS, Strasbourg, France (DOI: 10.26093/cds/vizier). The original description of the VizieR service was published in A&AS 143, 23.

*Facility:* CFHT.

*Software:* DAOPHOT (Stetson 1987, 2011), GALSIM (Rowe et al. 2015), IRAF (Tody 1986, 1993), ISHAPE (Larsen 1999), Matplotlib (Hunter 2007), NumPy (Harris et al. 2020), PSFEx (Bertin 2011), SAOImage (Joye & Mandel 2003), SciPy (Virtanen et al. 2020), SExtractor (Bertin & Arnouts 1996), SuperMongo (Lupton & Monger 1991), TOPCAT (Taylor 2005).

## Appendix

We determine the  $M_*$  versus  $N_{\text{GC}}$  correlation for the sample in Table 15. We use the galaxy types in Sahu et al. (2019b; Column 3), which are based on the classification grid of Graham (2019). We obtain separate fits for ellipticals (E), lenticulars (L), and spirals (S), with the FITEXY regression routines (Press et al. 1992), as modified by Tremaine et al. (2002) and Novak et al. (2006) to allow for the addition of intrinsic (or *cosmic*) scatter in the parameters. Summarizing, if data pairs  $(x_i, y_i)$  with individual measurement uncertainties

$(\sigma_{x,i}, \sigma_{y,i})$  are related by the linear equation  $y = \alpha + \beta x$ , the expression to minimize is

$$\chi^2 = \sum \frac{y_i - \alpha - \beta(x_i - \langle x \rangle)^2}{(\sigma_{y,i}^2 + \epsilon_y^2) + \beta^2(\sigma_{x,i}^2 + \epsilon_x^2)}, \quad (\text{A1})$$

where  $\langle x \rangle \equiv N^{-1} \sum_{i=1}^N x_i$  is the sample mean, and  $\epsilon_x$  and  $\epsilon_y$  represent the additional intrinsic scatter over the formal measurement errors. If additional cosmic scatter indeed exists, as implied by a reduced  $\chi^2_\nu > 1$ , the epsilons can be increased until  $\chi^2_\nu = 1$ . We searched for solutions both assuming  $\epsilon_x = 0$ , with all additional scattering in  $y$ , and distributing the potential supplemental scattering between  $\epsilon_x$  and  $\epsilon_y$ . In the absence of other constraints, when epsilons are added simultaneously to the  $M_*$  and  $N_{\text{GC}}$  values, their squares are kept in the same ratio observed when only  $\epsilon_y$  is appended to either variable.

Correlation solutions with the FITEXY routines are shown in Table 16. We also carry out fits with the BCES method by Akritas & Bershady (1996), with results for the bisector line of the forward ( $Y|X$ ) and inverse ( $X|Y$ ) regressions presented in Table 17. The solutions have the form  $Y = \alpha + \beta(X - \langle x \rangle)$ . To note: lenticular galaxies do show a correlation.

We perform analogous fits to  $M_*$  versus  $M_*$ , for E, S, and E+S galaxies. The solutions are listed in Tables 18 and 19.

**Table 15**  
Properties of Galaxies Used in the Fits

Galaxy	Type1	Type2	$d$ (Mpc)	$N_{\text{GC}}$	$\Delta N_{\text{GC}}$	$\log M_{\star}/M_{\odot}$
NGC 221	E2		0.8	10		6.46(+0.08, -0.10)
NGC 4486A	E2	E	15.6	21		7.15(+0.13, -0.11)
NGC 821	E4	E	24.1	320		8.23(+0.16, -0.25)
NGC 1332	S0	ES	22.9	1000	500	9.17(+0.06, -0.06)
NGC 1399	E1	E	20.0	6625	1180	8.69(+0.06, -0.07)
NGC 3377	E5	E	11.2	266	66	8.25(+0.19, -0.29)
NGC 3379	E1	E	10.6	270	68	8.04(+0.22, -0.26)
NGC 3414	S0	E	25.2	400	200	9.40(+0.06, -0.08)
NGC 3585	S0	E	20.0	300	100	8.51(+0.15, -0.13)
NGC 3607	E	E	22.8	600	200	8.15(+0.10, -0.15)
NGC 3608	E2	E	22.9	450	200	8.67(+0.09, -0.10)
NGC 3842	E	E	98.4	9850	3900	9.99(+0.11, -0.13)
NGC 4261	E2	E	31.6	530	100	8.71(+0.08, -0.09)
NGC 4291	E2	E	26.2	1200	600	8.98(+0.10, -0.18)
NGC 4350	S0	EBS	15.4	196	60	8.74(+0.10, -0.10)
NGC 4374	E1	E	18.4	4300	1200	8.96(+0.05, -0.04)
NGC 4472	E2	E	16.3	7800	850	9.26(+0.12, -0.18)
NGC 4473	E5	E	15.7	376	97	7.95(+0.19, -0.29)
NGC 4486	E0	E	16.1	13300	2000	9.77(+0.03, -0.03)
NGC 4552	E1	E	15.3	1200	250	8.68(+0.04, -0.05)
NGC 4621	E4	E	18.3	800	355	8.60(+0.06, -0.07)
NGC 4649	E2	E	16.8	4745	1100	9.63(+0.09, -0.11)
NGC 4697	E6	E	11.7	229	50	8.28(+0.08, -0.10)
NGC 4889	E	E	103.2	11000	1340	10.32(+0.25, -0.54)
NGC 5846	E0	E	24.9	4700	1200	9.04(+0.07, -0.09)
NGC 6086	E	E	132.0	4584	1362	9.56(+0.16, -0.16)
NGC 7768	E	E	112.8	3000	1300	9.11(+0.15, -0.27)
IC 1459	E4	E	29.2	2000	800	9.45(+0.14, -0.25)
IC 4296	BCG		50.8	6400	1600	9.13(+0.06, -0.07)
NGC 5845	E3	ES	25.9	140	70	8.69(+0.12, -0.16)
NGC 4382	E2		18.4	1100	181	7.81
A2052	BCG		141.0	27000	9000	9.66
NGC 4486B	E1	E	16.3	15		9.00
NGC 5128	E0p	S0merg	3.8	1300	300	7.71(+0.13, -0.19)
NGC 1023	SB0	SB0	11.4	221	100	7.64(+0.04, -0.04)
NGC 1316	E	SAB0merg	21.5	647	100	8.24(+0.17, -0.23)
NGC 2778	E2	S0	22.9	50	30	7.15(+0.30, -0.30)
NGC 3115	S0	S0	9.7	550	150	8.96(+0.19, -0.15)
NGC 3384	SB0	S0	11.6	128	100	7.04(+0.16, -0.26)
NGC 4459	E2	S0	16.1	218	28	7.84(+0.08, -0.08)
NGC 4564	S0	S0	15.0	213	31	7.92(+0.10, -0.14)
NGC 5813	E2	S0	32.2	1650	400	8.84(+0.07, -0.07)
NGC 7332	S0	SB0	23.0	175	15	7.11(+0.17, -0.21)
NGC 7457	S0	S0	13.2	178	75	7.00(+0.20, -0.40)
NGC 224	Sb	SBb	0.7	450	100	8.18(+0.20, -0.10)
NGC 253	SBC	SABC	3.4	92	21	6.70(+0.30, -0.30)
NGC 3031	Sb	SABab	3.6	172	100	7.84(+0.11, -0.06)
NGC 3368 <sup>a b</sup>		SABA	10.4	35	18	6.88(+0.09, -0.09)
NGC 4258 <sup>a c</sup>		SABB	7.6	105	40	7.60(+0.01, -0.01)
NGC 4395 <sup>a d</sup>		SBM	4.3	15	7	5.56(+0.13, -0.13)
NGC 4594	Sa	Sa	9.8	1900	300	8.72(+0.30, -0.57)
NGC 4736 <sup>a b</sup>		SABab	5.0	46	18	6.83(+0.10, -0.10)
NGC 4826 <sup>a b</sup>		Sab	7.3	69	30	6.20(+0.11, -0.11)
MW	Sbc	SBbc	0.0	160	10	6.61(+0.04, -0.04)

**Notes.** Galaxy sample from Harris et al. (2014); data from references therein. Column 3: galaxy types from Sahu et al. (2019b), based on the classification grid of Graham (2019).

<sup>a</sup> These galaxies were not in the original sample.  $N_{\text{GC}}$  from González-Lópezlira et al. (2017, 2019), this work.

<sup>b</sup>  $M_{\star}$  from Kormendy & Ho (2013).

<sup>c</sup>  $M_{\star}$  from Humphreys et al. (2013).

<sup>d</sup>  $M_{\star}$  from Peterson et al. (2005).

Galaxies NGC221, NGC4486A, NGC4486B, NGC4382, A2052 (upper limits), NGC5845, NGC5128 (outliers and/or large uncertainties) are excluded from the fits.

**Table 16**  
Correlation Solutions with FITEXY

Solutions for:	Sample	N	$\alpha$ dex	$\beta$	$\langle x \rangle$ dex	$\epsilon_y$ dex	$\epsilon_x$ dex	$\chi^2_\nu$	rms dex
log $M_*$ versus log $N_{\text{GC}}$	E	27	8.871 ± 0.029	0.915 ± 0.051	3.2	0	0	6.9	0.403
			8.963 ± 0.074	0.771 ± 0.130	3.2	0.35	0	1.0	0.378
			8.967 ± 0.080	0.972 ± 0.158	3.2	0.26	0.27	1.0	0.396
	S	10	6.455 ± 0.080	2.394 ± 0.261	2.1	0	0	6.2	0.964
			7.086 ± 0.164	1.515 ± 0.310	2.1	0.42	0	1.0	0.444
			7.077 ± 0.170	1.673 ± 0.329	2.1	0.32	0.17	1.0	0.464
	L	10	7.802 ± 0.072	1.617 ± 0.243	2.4	0	0	2.6	0.374
			7.767 ± 0.127	1.617 ± 0.342	2.4	0.28	0	1.0	0.372
			7.752 ± 0.133	1.776 ± 0.388	2.4	0.21	0.12	1.0	0.387
log $N_{\text{GC}}$ versus log $M_*$	E	27	3.232 ± 0.032	1.093 ± 0.061	8.9	0	0	6.9	0.440
			3.138 ± 0.077	0.815 ± 0.136	8.9	0.36	0	1.0	0.378
			3.132 ± 0.082	1.029 ± 0.166	8.9	0.27	0.26	1.0	0.407
	S	10	2.334 ± 0.030	0.418 ± 0.045	7.1	0	0	6.2	0.403
			2.083 ± 0.098	0.534 ± 0.103	7.1	0.25	0	1.0	0.273
			2.080 ± 0.101	0.598 ± 0.118	7.1	0.17	0.32	1.0	0.277
	L	10	2.398 ± 0.045	0.618 ± 0.093	7.8	0	0	2.6	0.231
			2.434 ± 0.071	0.509 ± 0.116	7.8	0.16	0	1.0	0.213
			2.427 ± 0.073	0.564 ± 0.123	7.8	0.12	0.21	1.0	0.218

**Table 17**  
Correlation Solutions with BCES

Solutions for:	Sample	N	$\alpha$ dex	$\beta$	$\langle x \rangle$ dex	$\epsilon_y$ dex	$\epsilon_x$ dex	$\chi^2_\nu$	rms dex
log $M_*$ versus log $N_{\text{GC}}$	E	27	8.980 ± 0.078	1.000 ± 0.098	3.2	0	0	7.8	0.400
			8.980 ± 0.074	0.803 ± 0.126	3.2	0.35	0	1.0	0.378
			8.992 ± 0.079	1.010 ± 0.126	3.2	0.26	0.27	1.0	0.403
	S	10	7.110 ± 0.146	1.660 ± 0.218	2.1	0	0	20.9	0.460
			7.128 ± 0.139	1.470 ± 0.182	2.1	0.42	0	1.0	0.441
			7.118 ± 0.144	1.640 ± 0.237	2.1	0.32	0.17	1.0	0.457
	L	10	7.760 ± 0.126	1.850 ± 0.447	2.4	0	0	2.7	0.398
			7.758 ± 0.119	1.670 ± 0.418	2.4	0.28	0	1.0	0.376
			7.750 ± 0.126	1.850 ± 0.496	2.4	0.21	0.12	1.0	0.398
log $N_{\text{GC}}$ versus log $M_*$	E	27	3.114 ± 0.072	0.787 ± 0.089	8.9	0.36	0	1.0	0.377
	S	10	2.063 ± 0.086	0.532 ± 0.101	7.1	0.25	0	1.0	0.272
	L	10	2.413 ± 0.067	0.485 ± 0.142	7.8	0.16	0	1.0	0.212

**Table 18**  
Correlation Solutions with FITEXY for  $M_*$  and Total Galaxy Mass

Solutions for:	Sample	N	$\alpha$ dex	$\beta$	$\langle x \rangle$ dex	$\epsilon_y$ dex	$\epsilon_x$ dex	$\chi^2_\nu$	rms dex
log $M_*$ versus log $M_*$	E	27	8.812 ± 0.035	1.369 ± 0.086	11.1	0	0	5.5	0.411
			8.915 ± 0.075	1.141 ± 0.190	11.1	0.34	0	1.0	0.380
			8.906 ± 0.080	1.416 ± 0.228	11.1	0.25	0.18	1.0	0.399
	S	10	5.472 ± 0.203	3.065 ± 0.418	10.0	0	0	10.0	2.34
			7.092 ± 0.183	1.028 ± 0.262	10.0	0.51	0	1.0	0.502
			7.077 ± 0.196	1.238 ± 0.310	10.0	0.37	0.30	1.0	0.535
	E+S	37	7.865 ± 0.040	2.425 ± 0.082	10.8	0	0	8.8	1.082
			8.425 ± 0.082	1.390 ± 0.129	10.8	0.43	0	1.0	0.475
			8.407 ± 0.085	1.556 ± 0.146	10.8	0.31	0.20	1.0	0.322
log $M_*$ versus log $M_*$	E	27	11.224 ± 0.024	0.730 ± 0.046	8.9	0	0	5.5	0.300
			11.153 ± 0.053	0.567 ± 0.094	8.9	0.24	0	1.0	0.263
			11.154 ± 0.056	0.706 ± 0.113	8.9	0.18	0.25	1.0	0.282
	S	10	10.585 ± 0.027	0.327 ± 0.045	7.1	0	0	10.0	0.763
			10.084 ± 0.150	0.678 ± 0.168	7.1	0.41	0	1.0	0.422
			10.076 ± 0.157	0.807 ± 0.202	7.1	0.30	0.37	1.0	0.432
	E+S	37	11.077 ± 0.016	0.413 ± 0.014	8.4	0	0	8.8	0.446
			10.869 ± 0.053	0.576 ± 0.054	8.4	0.27	0	1.0	0.320
			10.861 ± 0.054	0.643 ± 0.060	8.4	0.20	0.31	1.0	0.500

**Table 19**  
Correlation Solutions with BCES for  $M_*$  and Total Galaxy Mass

Solutions for:	Sample	$N$	$\alpha$ dex	$\beta$	$\langle x \rangle$ dex	$\epsilon_y$ dex	$\epsilon_x$ dex	$\chi^2_\nu$	rms dex
$\log M_*$ versus $\log M_*$	E	27	$8.960 \pm 0.078$	$1.460 \pm 0.149$	11.1	0	0	5.5	0.405
			$8.955 \pm 0.073$	$1.190 \pm 0.183$	11.1	0.34	0	1.0	0.381
			$8.952 \pm 0.078$	$1.480 \pm 0.184$	11.1	0.25	0.18	1.0	0.407
	S	10	$7.151 \pm 0.167$	$1.220 \pm 0.135$	10.0	0	0	10.0	0.530
			$7.090 \pm 0.158$	$1.000 \pm 0.131$	10.0	0.51	0	1.0	0.501
			$7.081 \pm 0.166$	$1.210 \pm 0.163$	10.0	0.37	0.30	1.0	0.527
	E+S	37	$8.390 \pm 0.080$	$1.500 \pm 0.140$	10.8	0	0	8.8	0.491
			$8.469 \pm 0.078$	$1.380 \pm 0.131$	10.8	0.43	0	1.0	0.475
			$8.420 \pm 0.080$	$1.500 \pm 0.153$	10.8	0.31	0.20	1.0	0.488
$\log M_*$ versus $\log M_*$	E	27	$11.134 \pm 0.050$	$0.543 \pm 0.062$	8.9	0.24	0	1.0	0.262
	S	10	$10.042 \pm 0.133$	$0.681 \pm 0.128$	7.1	0.41	0	1.0	0.420
	E+S	37	$10.837 \pm 0.052$	$0.611 \pm 0.070$	8.4	0.27	0	1.0	0.318

## ORCID IDs

- Rosa A. González-Lópezlira <https://orcid.org/0000-0003-1557-4931>  
Luis Lomelí-Núñez <https://orcid.org/0000-0003-2127-2841>  
Yasna Ordenes-Briceño <https://orcid.org/0000-0001-7966-7606>  
Laurent Loinard <https://orcid.org/0000-0002-5635-3345>  
Stephen Gwyn <https://orcid.org/0000-0001-8221-8406>  
Karla Alamo-Martínez <https://orcid.org/0000-0002-5897-7813>  
Gustavo Bruzual <https://orcid.org/0000-0002-6971-5755>  
Ariane Lançon <https://orcid.org/0000-0002-7214-8296>  
Thomas H. Puzia <https://orcid.org/0000-0003-0350-7061>

## References

- Agertz, O., Teyssier, R., & Moore, B. 2009, *MNRAS*, **397**, L64  
Akritas, M. G., & Bershady, M. A. 1996, *ApJ*, **470**, 706  
Ashman, K. M., & Zepf, S. E. 1992, *ApJ*, **384**, 50  
Ashman, K. M., & Zepf, S. E. 1998, in *Globular Cluster Systems*, ed. K. M. Ashman & E. Zepf (New York: Cambridge Univ. Press)  
Athanassoula, E. 2005, *MNRAS*, **358**, 1477  
Baes, M., Buyle, P., Hau, G. K. T., & Dejonghe, H. 2003, *MNRAS*, **341**, L44  
Bertin, E. 2011, in *ASP Conf. Proc.* 442, *Astronomical Data Analysis Software and Systems XX*, ed. I. N. Evans et al. (San Francisco, CA: ASP), 435  
Bertin, E., & Arnouts, S. 1996, *A&AS*, **117**, 393  
Blakeslee, J. P., Cantiello, M., Mei, S., et al. 2010, *ApJ*, **724**, 657  
Blakeslee, J. P., Tonry, J. L., & Metzger, M. R. 1997, *AJ*, **114**, 482  
Blecha, A. 1986, *A&A*, **154**, 321  
Bogdán, Á., Lovisari, L., Volonteri, M., et al. 2018, *ApJ*, **852**, 131  
Boulade, O., Charlot, X., Abbon, P., et al. 2003, *Proc. SPIE*, **4841**, 72  
Bruzual, G., & Charlot, S. 2003, *MNRAS*, **344**, 1000  
Burkert, A., & Forbes, D. A. 2020, *AJ*, **159**, 56  
Burkert, A., & Tremaine, S. 2010, *ApJ*, **720**, 516  
Capuzzo-Dolcetta, R., & Donnarumma, I. 2001, *MNRAS*, **328**, 645  
Capuzzo-Dolcetta, R., & Mastrobuono-Battisti, A. 2009, *A&A*, **507**, 183  
Capuzzo-Dolcetta, R., & Vicari, A. 2005, *MNRAS*, **356**, 899  
Chabrier, G. 2003, *PASP*, **115**, 763  
Côté, P., Marzke, R. O., & West, M. J. 1998, *ApJ*, **501**, 554  
Cowie, L. L., Hu, E. M., & Songaila, A. 1995, *Natur*, **377**, 603  
Davis, B. L., Graham, A. W., & Cameron, E. 2018, *ApJ*, **869**, 113  
Davis, B. L., Graham, A. W., & Cameron, E. 2019a, *ApJ*, **873**, 85  
Davis, B. L., Graham, A. W., & Combes, F. 2019b, *ApJ*, **877**, 64  
de Vaucouleurs, G., de Vaucouleurs, A., Corwin, H. G., Jr., et al. 1991, in *Third Reference Catalogue of Bright Galaxies*, ed. A. Corwin, H. G. Buta, Jr., R. J. Paturel, & G. Fouqué, Vol. I, II, and III (New York: Springer), 2091  
Desai, S., Armstrong, R., Mohr, J. J., et al. 2012, *ApJ*, **757**, 83  
Dressler, A. 1989, in *IAU Symp.* 134, *Active Galactic Nuclei*, ed. D. E. Osterbrock & J. S. Miller (Dordrecht: Kluwer Academic), 217  
Fabian, A. C. 2012, *ARA&A*, **50**, 455  
Ferrarese, L. 2002, *ApJ*, **578**, 90  
Ferrarese, L., & Merritt, D. 2000, *ApJ*, **539**, L9  
Filippenko, A. V., & Ho, L. C. 2003, *ApJL*, **588**, L13  
Forbes, D. A., Read, J. I., Gieles, M., & Collins, M. L. M. 2018, *MNRAS*, **481**, 5592  
Gebhardt, K., Bender, R., Bower, G., et al. 2000, *ApJ*, **539**, L13  
Georgiev, I. Y., Puzia, T. H., Goudfrooij, P., et al. 2010, *MNRAS*, **406**, 1967  
Gnedin, O. Y., Ostriker, J. P., & Tremaine, S. 2014, *ApJ*, **785**, 71  
González-Lópezlira, R. A., Lomelí-Núñez, L., & Álamo-Martínez, K. 2017, *ApJ*, **835**, 184  
González-Lópezlira, R. A., Mayya, Y. D., Loinard, L., et al. 2019, *ApJ*, **876**, 39  
Goudfrooij, P., Strader, J., Brenneman, L., et al. 2003, *MNRAS*, **343**, 665  
Graham, A. W. 2012, *ApJ*, **746**, 113  
Graham, A. W. 2019, *MNRAS*, **487**, 4995  
Graham, A. W., & Scott, N. 2013, *ApJ*, **764**, 151  
Graham, A. W., & Spitler, L. R. 2009, *MNRAS*, **397**, 2148  
Guo, Y., Ferguson, H. C., Bell, E. F., et al. 2015, *ApJ*, **800**, 39  
Gwyn, S. D. J. 2008, *PASP*, **120**, 212  
Gwyn, S. D. J. 2014, in *ASP Conf. Ser.* 485, *Astronomical Data Analysis Software and Systems XXIII*, ed. N. Manset & P. Forshay (San Francisco, CA: ASP), 387  
Häring, N., & Rix, H.-W. 2004, *ApJ*, **604**, L89  
Harris, C. R., Millman, K. J., van der Walt, S. J., et al. 2020, *Natur*, **585**, 357  
Harris, G. L. H., & Harris, W. E. 2011, *MNRAS*, **410**, 2347  
Harris, G. L. H., Poole, G. B., & Harris, W. E. 2014, *MNRAS*, **438**, 2117  
Harris, W. E. 1996, *AJ*, **112**, 1487  
Harris, W. E., Blakeslee, J. P., & Harris, G. L. H. 2017, *ApJ*, **836**, 67  
Harris, W. E., Harris, G. L. H., & Alessi, M. 2013, *ApJ*, **772**, 82  
Harris, W. E., Kavelaars, J. J., Hanes, D. A., Pritchett, C. J., & Baum, W. A. 2009, *AJ*, **137**, 3314  
Hudson, M. J., Harris, G. L., & Harris, W. E. 2014, *ApJL*, **787**, L5  
Humphreys, E. M. L., Reid, M. J., Moran, J. M., Greenhill, L. J., & Argon, A. L. 2013, *ApJ*, **775**, 13  
Hunter, J. D. 2007, *CSE*, **9**, 90  
Jahnke, K., & Macciò, A. V. 2011, *ApJ*, **734**, 92  
Jalocha, J., Bratek, Ł., & Kutschera, M. 2008, *ApJ*, **679**, 373  
Jordán, A., McLaughlin, D. E., Côté, P., et al. 2007, *ApJS*, **171**, 101  
Joye, W. A., & Mandel, E. 2003, in *ASP Conf. Ser.* 295, *Astronomical Data Analysis Software and Systems XII*, ed. H. E. Payne, R. I. Jedrzejewski, & R. N. Hook (San Francisco, CA: ASP), 489  
King, I. 1962, *AJ*, **67**, 471  
King, I. R. 1966, *AJ*, **71**, 64  
Kissler-Patig, M., Ashman, K. M., Zepf, S. E., & Freeman, K. C. 1999, *AJ*, **118**, 197  
Kormendy, J. 1993, in *IAU Symp.* 153, *Galactic Bulges*, ed. H. DeJonghe & H. J. Habing (Dordrecht: Kluwer Academic), 209  
Kormendy, J. 2013, in *Secular Evolution of Galaxies*, ed. J. Falcón-Barroso & J. H. Knapen (Cambridge: Cambridge Univ. Press), 1  
Kormendy, J., & Bender, R. 2011, *Natur*, **469**, 377  
Kormendy, J., Bender, R., & Cornell, M. E. 2011, *Natur*, **469**, 374  
Kormendy, J., Drory, N., Bender, R., et al. 2010, *ApJ*, **723**, 54  
Kormendy, J., & Ho, L. C. 2013, *ARA&A*, **51**, 511  
Kormendy, J., & Kennicutt, R. C. 2004, *ARA&A*, **42**, 603  
Kormendy, J., & Richstone, D. 1995, *ARA&A*, **33**, 581

- Kravtsov, A. V., & Gnedin, O. Y. 2005, *ApJ*, **623**, 650
- Kron, R. G. 1980, *ApJS*, **43**, 305
- Kruijssen, J. M. D. 2015, *MNRAS*, **454**, 1658
- Larsen, S. S. 1999, *A&AS*, **139**, 393
- Lupton, R., & Monger, P. 1991, unpublished paper
- Magorrian, J., Tremaine, S., Richstone, D., et al. 1998, *AJ*, **115**, 2285
- Martin, G., Kaviraj, S., Volonteri, M., et al. 2018, *MNRAS*, **476**, 2801
- McLaughlin, D. E., Harris, W. E., & Hanes, D. A. 1994, *ApJ*, **422**, 486
- Muñoz, R. P., Puzia, T. H., Lançon, A., et al. 2014, *ApJS*, **210**, 4
- Novak, G. S., Faber, S. M., & Dekel, A. 2006, *ApJ*, **637**, 96
- Oke, J. B. 1974, *ApJS*, **27**, 21
- Olsen, K. A. G., Miller, B. W., Suntzeff, N. B., et al. 2004, *AJ*, **127**, 2674
- Peng, C. Y. 2007, *ApJ*, **671**, 1098
- Peterson, B. M., Bentz, M. C., Desroches, L.-B., et al. 2005, *ApJ*, **632**, 799
- Powalka, M., Lançon, A., Puzia, T. H., et al. 2016, *ApJS*, **227**, 12
- Press, W. H., Teukolsky, S. A., Vetterling, W. T., & Flannery, B. P. 1992, *Numerical Recipes in FORTRAN. The Art of Scientific Computing* (2nd ed; Cambridge: Cambridge Univ. Press)
- Puget, P., Stadler, E., Doyon, R., et al. 2004, *Proc. SPIE*, **5492**, 978
- Reid, M. J., Menten, K. M., Brunthaler, A., et al. 2014, *ApJ*, **783**, 130
- Reines, A. E., & Volonteri, M. 2015, *ApJ*, **813**, 82
- Rowe, B. T. P., Jarvis, M., Mandelbaum, R., et al. 2015, *A&C*, **10**, 121
- Sahu, N., Graham, A. W., & Davis, B. L. 2019a, *ApJ*, **876**, 155
- Saburova, A. S., Shaldenkova, E. S., & Zasov, A. V. 2009, *ARep*, **53**, 801
- Sahu, N., Graham, A. W., & Davis, B. L. 2019b, *ApJ*, **887**, 10
- Sauvaget, T., Hammer, F., Puech, M., et al. 2018, *MNRAS*, **473**, 2521
- Savorgnan, G. A. D., Graham, A. W., Marconi, A., et al. 2016, *ApJ*, **817**, 21
- Schlafly, E. F., & Finkbeiner, D. P. 2011, *ApJ*, **737**, 103
- Schweizer, F. 1987, in *Nearly Normal Galaxies. From the Planck Time to the Present*, Santa Cruz Summer Workshops in Astronomy and Astrophysics, ed. S. M. Faber (New York: Springer), **18**
- Scott, N., Graham, A. W., & Schombert, J. 2013, *ApJ*, **768**, 76
- Sérsic, J. L. 1963, *BAAA*, **6**, 41
- Seth, A. C., Cappellari, M., Neumayer, N., et al. 2010, *ApJ*, **714**, 713
- Silk, J., & Rees, M. J. 1998, *A&A*, **331**, L1
- Simmons, B. D., Smethurst, R. J., & Lintott, C. 2017, *MNRAS*, **470**, 1559
- Smethurst, R. J., Simmons, B. D., Lintott, C. J., & Shanahan, J. 2019, *MNRAS*, **489**, 4016
- Spitler, L. R., & Forbes, D. A. 2009, *MNRAS*, **392**, L1
- Stetson, P. B. 1987, *PASP*, **99**, 191
- Stetson, P. B. 2011, DAOPHOT: Crowded-field Stellar Photometry Package, *Astrophysics Source Code Library*, ascl:[1104.011](#)
- Taylor, M. B. 2005, in *ASP Conf. Ser. 347, Astronomical Data Analysis Software and Systems XIV*, ed. P. L. Shopbell, M. C. Britton, & R. Ebert (San Francisco, CA: ASP), **29**
- Thim, F., Hoessel, J. G., Saha, A., et al. 2004, *AJ*, **127**, 2322
- Tody, D. 1986, *Proc. SPIE*, **627**, 733
- Tody, D. 1993, in *ASP Conf. Ser. 52, Astronomical Data Analysis Software and Systems II*, ed. R. J. Hanisch, R. J. V. Brissenden, & J. Barnes (San Francisco, CA: ASP), **173**
- Tonry, J. L., Dressler, A., Blakeslee, J. P., et al. 2001, *ApJ*, **546**, 681
- Tremaine, S., Gebhardt, K., Bender, R., et al. 2002, *ApJ*, **574**, 740
- Turner, M. L., Côté, P., Ferrarese, L., et al. 2012, *ApJS*, **203**, 5
- van den Bosch, R. C. E. 2016, *ApJ*, **831**, 134
- Virtanen, P., Gommers, R., Oliphant, T. E., et al. 2020, *NatMe*, **17**, 261
- Wang, S., Ma, J., Wu, Z., & Zhou, X. 2014, *AJ*, **148**, 4